bioRxiv preprint doi: https://doi.org/10.1101/092486; this version posted December 8, 2016. The copyright holder for this preprint (which was not certified by peer review) is the author/funder, who has granted bioRxiv a license to display the preprint in perpetuity. It is made available under aCC-BY-ND 4.0 International license.

The architectural balance of the Ventral Nerve Cord depends on the level of JNK signaling activity

Katerina Karkali[1 2 3], George Panayotou[2], Timothy E. Saunders[3] and Enrique Martín-Blanco[1 3 *]

1. Instituto de Biología Molecular de Barcelona (CSIC), Parc Cientific de Barcelona, Baldiri Reixac 10-12, 08028 Barcelona, Spain

2. BSRC Alexander Fleming, 34 Fleming Street, 16672 Vari, Greece

3. Mechanobiology Institute, 5 Engineering Drive 1, National University of Singapore, 117411 Singapore

* Correspondence to: embbmc@ibmb.csic.es

Abstract

The segmented nervous system of bilaterians is organized in structural and functional modules. Modules share across species a robust structural stability. How this robustness is acquired during development is currently unknown. Here, we investigate the sequence of events involved in the establishment of the architectural balance of the nervous system. We demonstrate that a unique robustness pattern is common to the arthropods nervous system plan. This pattern depends on the fine control of the JNK signaling in a subset of early-specified pioneer neurons. JNK activity affects the level of expression of cell adhesion molecules (Fas 2), in part through the modulation of the transcription factor *zfh1*. A deficit in Fas 2 affects the fasciculation of the axons of primary neurons, leading to secondary bundling defects that result in a general reduction in spatial correlations. Failure to fasciculate affects both architectural robustness and tensional balance, ultimately impeding nervous system condensation.

bioRxiv preprint doi: https://doi.org/10.1101/092486; this version posted December 8, 2016. The copyright holder for this preprint (which was not certified by peer review) is the author/funder, who has granted bioRxiv a license to display the preprint in perpetuity. It is made available under aCC-BY-ND 4.0 International license.

INTRODUCTION

Modularity is common in the Central Nervous System (CNS) of both vertebrates and invertebrates (Leise, 1990) (Chen, Hall et al., 2006) (Redies & Puelles, 2001) and serves as an anatomical base for distributed function. In terms of efficiency, neural modules may be viewed as solutions that minimize wiring cost, following the wiring optimization principle postulated by Ramón y Cajal (Cajal, 1899). Wiring cost arises from metabolic requirements, signal delay and attenuation, and possible guidance defects (Tessier-Lavigne & Goodman, 1996). Whatever the origin of the wiring cost, it increases with the distance between connected neurons. Among various functionally equivalent arrangements, the one having the closest-connected neurons is assumed to be the most strongly selected (Chklovskii & Koulakov, 2004). Despite more than 100 years of intensive study, the mechanisms that guide the neural organization into modules and implement wiring optimization during development remain uncharacterized.

Modules vary in cell type and number across species, but for equivalent anatomical entities they share similarity in internal design and operation (Sporns & Betzel, 2016). This robust structural stability - given the complex architecture of the mature CNS - is a remarkable property, yet we have relatively little knowledge about how such robustness is achieved. Here, we present new insights into the sequence of developmental events involved in the establishment of the CNS architectural robustness.

It is known that tension forces contribute to various aspects of neuronal morphology and connectivity (Franze, 2013), including stabilization of neurite connections (Siechen, Yang et al., 2009). Secondly, mechanical tension may lead to the shortening of neuronal processes, thus contributing to compactness and functional wiring (Van Essen, 1997). Hence, mechanical tension in and along neuronal axons potentially contributes not only to regulation of neuronal function but ultimately to neural network module formation. In this scenario, the spatio-temporal regulation of tension can coordinate compaction and clustering of cells in the CNS (Siechen et al., 2009) and an obvious candidate to modulate this tension is the stress activated Jun N-terminal kinase (JNK) cascade (Hsieh & Nguyen, 2005). JNK signaling is a key element in regulating glia in vertebrates and *Jnk1*$^{-}$*; Jnk2*$^{-}$ mice fail to complete neural tube closure, displaying exencephaly (Kuan, Yang et al., 1999) (Waetzig & Herdegen, 2004). In *Drosophila*, JNK (*basket* - *bsk*) participates in controlling axonal growth (Srahna, Leyssen et al., 2006). Yet, the role of JNK signaling in the morphogenesis of the CNS remains poorly understood.

bioRxiv preprint doi: https://doi.org/10.1101/092486; this version posted December 8, 2016. The copyright holder for this preprint (which was not certified by peer review) is the author/funder, who has granted bioRxiv a license to display the preprint in perpetuity. It is made available under aCC-BY-ND 4.0 International license.

To unravel the mechanisms controlling how robust architectural stability and modularity are achieved during nervous system development, we focus on the arthropod CNS, in particular the Ventral Nerve Cord (VNC). The VNC of arthropods is composed of segmentally iterated ganglia within a particular three-dimensional architecture, with a stereotyped pattern of neurons. The positions of these neurons and their projections can be mapped employing segmentally repeated reference points (Landgraf, Sanchez-Soriano et al., 2003). The neuronal cell bodies are restricted to the cortex, while sensory axon and interneuron projections accumulate in the neuropile. Cohesive axon bundles build longitudinal connectives and establish transverse commissures (Technau, 2008).

Here, we focus on the communalities between the structural elements sustaining architectural stability, both in *Triops*, a branchiopod crustacean with indirect development and, in more detail, *Drosophila*, a highly derived insect. We employed correlative pan-axonal analysis to investigate the 3D architecture of the VNC and uncovered an iterated and conserved pattern of structural robustness (nodes) associated to architectural landmarks (commissures). We further identified Fasciclin 2 (Fas 2) axonal bundles in *Drosophila* as key contributors to the robustness of the VNC architecture and condensation. At a molecular level, proper structural patterning can be explained as a result of a delicate balance of JNK signaling activity in a few specific neurons. JNK governs the VNC structural equilibrium by non-autonomously controlling Fas 2 expression and, hence, axonal fasciculation (in part through the Zfh1 transcription factor). Together, these results elucidate essential molecular and cellular mechanisms underpinning robustness in the CNS architecture.

bioRxiv preprint doi: https://doi.org/10.1101/092486; this version posted December 8, 2016. The copyright holder for this preprint (which was not certified by peer review) is the author/funder, who has granted bioRxiv a license to display the preprint in perpetuity. It is made available under aCC-BY-ND 4.0 International license.

RESULTS

Modular Architecture of the Ventral Nerve Cord (VNC)

To study the architectural elements sustaining the VNC structural balance and to shed light on the evolutionary conservation level, we compared two species within Arthropoda with clearly recognizable VNC symmetry and covering a wide evolutive range: the branchiopod crustacean *Triops* has a less derived (plesiomorphic) nerve cord than insects (Harzsch, 2001), and *Drosophila* displays a complex fully evolved VNC. We first compared their mesoscopic VNCs organization by pan-axonal staining. In *Triops* the paired ganglia of each segment remained separated with somata-free commissures (Figure 1A, see also (Fritsch & Richter, 2010)), while in *Drosophila* well-structured commissures and prominent segmental and intersegmental nerves were apparent (Figure 1B and Movie S1). We then investigated spatial correlations within this topographical information. We uncovered two domains per segment (pan-axonal nodes) of high robustness (Figures 1C-1D) displaying a highly similar structural organization. Correlations decayed outside these domains as topographical noise increased (Figures 1E-1F). In summary, across insects and crustaceans, nodes appear to follow a double wave pattern, which is robustly sustained at precise cyclic positions alongside the anterior and posterior commissures.

Next, we asked how this highly conserved structural pattern of the VNC assembles. Amongst the most likely participating elements are the longitudinal connectives, which are built by fasciculation of axons with different origins. In *Drosophila*, a subset of these axons are immunoreactive for Fas 2, a neural cell adhesion molecule, whose loss-of-function lead to complete or partial connectives defasciculation (Lin, Fetter et al., 1994). To investigate the potential structural role of Fas 2 fascicles, we evaluated their spatial correlation (Figures 1G-1H, see also Movie S2). Contrary to the previously assumed even distribution of Fas 2 fascicles (Landgraf et al., 2003), they showed a structural pattern with a single robust node per segment, at an average internodal distance of 28 μm (Figure 1I). These nodes did not position at the same location as any of the pan-axonal nodes, but slightly posterior to the anterior commissure (see Figure S1). We confirmed this positional information by double staining with segmentally iterated markers (BP102 and 22C10), (Figure S2). At the nodes, the longitudinal connectives organize topographically in three compact fasciculated units in precise dorso-ventral/medio-lateral positions (internal, medial and external) (Figures 1J and S1). Outside the nodes, although

bioRxiv preprint doi: https://doi.org/10.1101/092486; this version posted December 8, 2016. The copyright holder for this preprint (which was not certified by peer review) is the author/funder, who has granted bioRxiv a license to display the preprint in perpetuity. It is made available under aCC-BY-ND 4.0 International license.

the Fas 2 axons always resolved in the same set of fascicles, noise drastically increased (Figure 1K). They spread in an imprecise distribution, reaching maximal randomness at the level of the posterior commissures (minimal correlation).

The correlation profiles of the Fas 2 connectives showed parametric periodicity (see Supplemental Experimental Procedures). They also showed a structural bias between the anterior/posterior organization of the connectives from the nodes (relative difference in the maximum and minimum spatial derivatives of aligned profiles) (Figure 1L). In other words, the structural noise for the Fas 2 fascicles increased steeply in the posterior direction towards a minimum correlation at the level of the posterior commissures recovering in a shallow gradient.

Robustness and modularity of the VNC architecture is regulated by JNK signaling levels

The JNK pathway stands as an obvious candidate to regulate VNC structural organization, considering its stress-related roles (Ip & Davis, 1998) and ability to increase developmental robustness (Adachi-Yamada, Fujimura-Kamada et al., 1999). In flies, JNK activity is modulated by a negative feedback loop implemented by the dual-specificity phosphatase Puckered (Puc). *puc* expression depends on Bsk activity and Bsk function is inhibited by Puc (Martin-Blanco, 1998). Although *puc* expression has been reported in the CNS (Martin-Blanco, Gampel et al., 1998), its function during morphogenesis is unknown. We found that in loss-of-function puc^{E69} mutants, the longitudinal connectives were highly defasciculated with the most lateral ones incompletely formed, and the intersegmental nerves unevenly spaced. Further, Fas 2 positive axons became irregularly recruited to more medial positions and, occasionally, the Fas 2 signal relocated to the cell bodies of particular neurons (aCC and pCC) (Figure 1M and Movie S3). Equivalent defects were also observed for puc^{B48}, another loss of function allele (Figure S3). puc^{E69} and puc^{B48} were generated by different transposon insertions in two different introns (Martin-Blanco et al., 1998).

In *puc* alleles, the Fas 2 fascicles became disorganized on the dorso-ventral/medio-lateral plane (Figure 1N). Single nodes of robust topographical organization were still present, with an increased average internodal distance of 33 μm (Figure 1O and S3), but the anterior/posterior bias of the correlation profiles was abolished (Figures 1L). The increased internodal distance in puc^{E69} (on average 18%) and puc^{B48} (39%) mutants affected VNC condensation. Direct

bioRxiv preprint doi: https://doi.org/10.1101/092486; this version posted December 8, 2016. The copyright holder for this preprint (which was not certified by peer review) is the author/funder, who has granted bioRxiv a license to display the preprint in perpetuity. It is made available under aCC-BY-ND 4.0 International license.

measurements of the VNC length in *puc*^{E69} and *puc*^{B48} further supported the condensation failure (Figure S4). In conclusion, Puc activity seems to be involved in the structural reinforcement and condensation of the VNC and not in the outlining of the segmental body plan.

Are the defects in fasciculation and VNC condensation in *puc* mutants a consequence of increased JNK activity? In the absence of the negative feedback loop mediated by *puc*, the level of JNK phosphorylation significantly rose in the developing VNC, re-locating in part to cell bodies (Figure 2), both for *puc*^{E69} (Figure 2B) and *puc*^{B48} (Figure 2C). This increase in JNK activity correlated with an increase in apoptosis over the basal cell death levels characteristic of the developing VNC (Figure S5).

In summary, a tight control of JNK signaling appears to be essential for the acquisition of the proper structural organization and architectural balance of the developing VNC. This control is exerted, at least in part, by Puc, which limits JNK activity and eventually prevents excessive cell death.

JNK signaling is dynamically regulated in the VNC during development

When and where is JNK activity controlled in the VNC? To answer this, we first studied the dynamics of *puc* expression, which is itself an early readout of JNK activity. A viable line expressing GFP under the control of the *puc*^{E69} enhancer identified a segmentally iterated subset of neurons at embryonic stage 17 (Figures 3A-3B). No cross-reaction was observed with glial markers (Figures 3C-3D and (Shklover, Mishnaevski et al., 2015)). This late pattern was the result of a cumulative process initiated at early stage 13 in a few neurons positioned along the VNC midline (Figure 3E and Movie S4). As development progressed, an increased number of neurons, both within the VNC and at the peripheral nervous system (PNS), expressed *puc*. We subsequently identified a minimum consensus comprising 19 *puc* positive neurons with varying intensity per hemisegment, (see representative diagrams in Figure 3F and Movie S5).

Dual staining of *puc*^{E69} embryos with neuronal markers [Even-skipped (Eve) and Engrailed (En)] identified most of the *puc*-expressing cells. Eve labeled the aCC, pCC, RP2, U1-U3 (plus weak/variable expression in U4-U5) and 3 out of the 8/10 ELC interneurons (Figures 4A-4C). Meanwhile, NL1, NL2, and iVUM5 neurons were En positive (Figures 4D-4F). Morphological and positional criteria further enabled the assignment of five Eve and En negative cells, AD,

bioRxiv preprint doi: https://doi.org/10.1101/092486; this version posted December 8, 2016. The copyright holder for this preprint (which was not certified by peer review) is the author/funder, who has granted bioRxiv a license to display the preprint in perpetuity. It is made available under aCC-BY-ND 4.0 International license.

ADV, dMP2 and 2 VUM En-negative motor neurons (Figures 4G-4H). This subset of *puc*-expressing neurons was largely conserved for puc^{B48} (Figure S6). puc^{B48} driven GFP expression was also restricted to neurons and in most cases also shared expression with Eve and En.

Summarizing, *puc* expression was detected from stage 13 in VUMs, pCC and possibly dMP2 neurons at the ventral midline. This expression pattern subsequently spreads out to diverse inter and motor neurons populating the longitudinal connectives and segmental and intersegmental nerves.

The level of JNK activity in specific *puc*-positive neurons determines the architectural balance of the VNC

The reduced architectural robustness of the VNC observed in *puc* could be the result of autonomous malfunction of the JNK pathway in the CNS, or just a structural consequence of the general disruption of embryo development. To investigate this, we generated JNK signaling loss- or gain-of-function conditions by overexpressing Bsk^{DN}, a dominant negative form of Bsk, or Hep^{CA}, a constitutively active form of Hemipterous (Hep), the *Drosophila* homologue of the JNK kinase MKK7. We targeted specific subsets of the *puc*-expressing cells employing different Gal4 lines (CQ2, RN2T and mzVUM).

The CQ2-Gal4 line drives expression of UAS-linked genes in the U1 to U5 motor neurons, a subset of Eve-positive neurons, which also express *puc* (Figure 5A). Neither the inhibition (Figure 5B), nor the hyperactivation of the JNK pathway (Figure 5C) resulted in any major alterations of the Fas 2 expressing connectives. The VNC architecture in both cases (e.g. node position and spatial correlation profiles) was similar to *wt* (Figures 1G-1I).

The RN2T-Gal4 line is specifically expressed in the *puc* positive aCC, pCC and RP2 neurons (Figure 5D). Interference with JNK signaling resulted in disorganization of Fas 2 connectives (Figure 5E). Intersegmental correlation became noisy and irregular and internodal distances expanded indicating a failure in condensation. On the other hand, the hyperactivation of the pathway, mimicking reduced *puc* levels, also strongly affected Fas 2 connectives, which kept a juvenile appearance (Figure 5F). In this case, although robust nodes were observed, the internodal distance enlarged and the VNC was lengthened.

The MzVum-Gal4 line is expressed, besides a few lateral cells, in the 3 VUM motor neurons

bioRxiv preprint doi: https://doi.org/10.1101/092486; this version posted December 8, 2016. The copyright holder for this preprint (which was not certified by peer review) is the author/funder, who has granted bioRxiv a license to display the preprint in perpetuity. It is made available under aCC-BY-ND 4.0 International license.

(Figure 5G). Bsk^{DN} expression slightly affected fasciculation of Fas 2 connectives (Figure 5H) but did not result in overt alterations in intersegmental correlations or internodal profiles. On the contrary, Hep^{CA} expression resulted in disorganization of Fas 2 connectives and increased noise in the spatial correlations (Figure 5I). Internodal distances became larger and localized spatial information was mostly lost.

All these data suggest that the level of JNK activity must be dynamically tuned in the early-specified aCC, pCC, and RP2 pioneers and VUM neurons to facilitate the robust organization of the VNC. The tuning of JNK activity depends on the transcriptional control of the dual specificity phosphatase Puc. This result cannot be ascribed to motor neuron activity, as the CQ cells did not participate.

JNK signaling modulates Fasciclin 2 levels in the developing VNC

JNK signaling modulates gene expression, cytoskeleton dynamics and cell adhesion (Davis, 2000). We aimed to explore whether the reduced architectural robustness of the VNC in *puc* mutants was a consequence of Fas 2 deregulation or subcellular mislocalization. By quantifying integrated densities in *wt*, puc^{E69}, and puc^{B48} embryos (Figures 6A-6C) we found that Fas 2 showed lower expression at the internodal versus the nodal domains in all conditions (Figure 6D), which points to an enriched axonal density at nodes. Remarkably, Fas 2 expression was consistently around 50% lower for both mutant conditions. We next quantified the relative Fas 2 protein levels present in stage 16 using full embryo extracts (Figure 6E). We found, again, a consistent reduction of expression levels in both mutant conditions. Together, these results indicate that the expression of Fas 2 is reduced in the absence of Puc and, hence, high JNK activity. This reduction was systemic and could not be assigned to individual domains within the VNC.

To determine how Fas 2 expression was controlled in response to JNK signaling, we searched for potential intermediate regulators. It has been recently shown that Fas 2 is downregulated in the VNC, and more specifically in the aCC and RP2 neurons in *zfh1* mutants (Zarin, Asadzadeh et al., 2014). Zfh1 is a Zn finger homeodomain family member expressed in all motor neurons, partially overlapping with *puc*. Further, Zfh1 is sufficient to promote transcription of Fas 2 in some interneurons. We hypothesized that JNK could (directly or indirectly) inhibit Zfh1,

bioRxiv preprint doi: https://doi.org/10.1101/092486; this version posted December 8, 2016. The copyright holder for this preprint (which was not certified by peer review) is the author/funder, who has granted bioRxiv a license to display the preprint in perpetuity. It is made available under aCC-BY-ND 4.0 International license.

resulting in Fas 2 expression reduction and, in the long run, in VNC disorganization.

In homozygous *zfh1* mutants, we found that the architectural robustness of the Fas 2 connectives was strongly affected and that the VNC displayed juvenile characteristics. Spatial correlations became noisier and internodal distance increased (Figure 7A). *zfh1* phenotype thus strongly resembles those of *puc* or Hep^{CA} overexpression. We also found that the averaged integrated Fas 2 density (node versus internode) was consistently lower for *zfh1* mutants (Figure 7B). The failure in architectural organization of the VNC in *zfh1* can be interpreted as a result of the systemic reduction of Fas 2, similarly as for *puc*. Therefore, we explored how *puc* and *zfh1* could relate to each other and found that Zfh1 expression was shut down in specific subsets of motor neurons, and systemically reduced in *puc* mutants (Figure 7C and S7 and Movie S6).

Altogether, these analyses support a model in which the architectural organization and condensation of the VNC are the result of the proper deployment of Fas 2 partly mediated by Zfh1 in response to the controlled activity of the JNK pathway in a particular set of pioneering neurons (at least aCC, pCC, RP2 and VUMs) (Figure 7D and Discussion).

bioRxiv preprint doi: https://doi.org/10.1101/092486; this version posted December 8, 2016. The copyright holder for this preprint (which was not certified by peer review) is the author/funder, who has granted bioRxiv a license to display the preprint in perpetuity. It is made available under aCC-BY-ND 4.0 International license.

DISCUSSION

The complex nervous system found in vertebrates and other bilaterians is thought to have emerged from an ancient, diffuse nerve plexus (Arendt, Tosches et al., 2016). Bilateralism arose as the ancestral single blastopore closed medially. The elongation of bilaterians was accompanied in annelids and arthropods by the segmentation of the body, and hence their nervous systems (Qing Yu, 2015). The arthropod CNS contains serially repeated 'homologous' neurons that function not only in different body segments but also across species. Here, we demonstrate that this conservation at the cellular level is reflected in a unique structural robustness pattern common to the VNC plan (Figure 1). Fasciculated axons become topographically organized at two anchoring positions per segment in a robust way at the level of the ganglions and the connecting anterior and posterior commissures. These ganglions and commissures contain bundles of primary neurites where most of the synapses are made. A likely reason for the striking robust conservation in the organization of the early nervous system is that it responds to conserved architectural needs (Matheson, 2002) (Arendt et al., 2016). It is fascinating that these homologous neurons, after 500 million years of evolutionary divergence, still organize architecturally in a similar manner.

The longitudinal Fas 2 fascicles have been employed as anatomical references to chart the neuropile: two medial, five intermedial, and three lateral fascicles. Fas 2 is initially expressed in the *puc*-positive aCC and pCC pioneer neurons which fasciculate in the medial region. Connectives develop from this initial seed, from medial to lateral, guiding the recruitment of ipsi- and contra-lateral axons (Landgraf et al., 2003) (Sanchez-Soriano, Tear et al., 2007) (Zlatic, Li et al., 2009). We found that the Fas 2 connectives organize topographically around a single robust node per segment, positioned just posterior to the anterior commissure (Figure 1, S1 and S2). We speculate that connectives work as structural beams and that the rear-ended arrangement of nodes acts to distribute more evenly any load from compression, tension or shear that could arise as the VNC is built, or that it may suffer once functional. This backbone will support the accumulated cargo of neuronal cell bodies, assuring the elements required to fulfill neural functions will stand up. Nonetheless, the Fas 2 connectives are only one element of the tensional network holding the VNC.

The balanced structural organization of the VNC is altered upon interference by JNK activity. Fas 2 bundles defasciculate, the overall shape of the neuropile is affected, and the VNC fails to

bioRxiv preprint doi: https://doi.org/10.1101/092486; this version posted December 8, 2016. The copyright holder for this preprint (which was not certified by peer review) is the author/funder, who has granted bioRxiv a license to display the preprint in perpetuity. It is made available under aCC-BY-ND 4.0 International license.

condense in *puc* mutants (Figures 1 and S4; see also Figure 7). The presence of a robust node per segment was unaltered, but internodal distances enlarged and spatial correlations were significantly noisier. Notably, the steeper slope posterior to the nodes of the spatial correlation profiles shallowed (Figure 1). This suggests that the shrinkage of this segmental domain is a relevant element for the condensation of the *wt* VNC along the antero-posterior axis.

In *Drosophila*, the pioneer neurons are specified and singled out at stage 9, initiating axonogenesis around stage 11 and culminating it in less than an hour (Jacobs & Goodman, 1989). In parallel, JNK activity builds up and *puc* expression initiates in the midline VUMs and the early pioneers pCC and dMP2 (Figures 3 and 4). This correlation suggests that the major aberrations observed in the fasciculation process in *puc* embryos result from pioneering defects. Potentially, inaccurate axonogenesis of pioneers could impact non-autonomously in the fasciculation of other axons from later neurons that subsequently encounter an altered guidance landscape. Failure of VNC condensation may have the same origin. While the growth cones of pioneer neurons navigate through the developing neuropile, the cell bodies they make contact with are also in motion. Altering JNK activity only in early-specified neurons and midline pioneers leads to widely spread fasciculation defects and affects the condensation of the whole neuropile (Figure 5). These defects are remarkably similar upon reduction or increment in JNK function, indicating that the precise control of its contribution is essential - the negative feedback loop mediated by *puc* is a main factor in this tight spatio-temporal regulation.

The regular segmental arrangement of Fas 2 nodes suggests they are important elements for the global stabilization of the structure of the VNC; nodes with conserved robust topography may serve as anchoring tensional posts. Defective node formation or alterations in their adhesion properties (e.g. by Fas 2 downregulation) weakens this structural scaffold. The disassembly of Fas 2 connectives and architectural rearrangements observed in *puc* mutants are associated with a strong reduction of Fas 2 levels. Remarkably, this reduction was not ascribed to the relocation of Fas 2 to different localizations (e.g. node to internode) but instead to its general systemic downregulation (Figure 6).

We have demonstrated that interfering with JNK activity in a small subset of neurons affects the expression of Fas 2 non-autonomously. How does JNK activity influence Fas 2? In *Drosophila* a network of transcription factors, comprised of Eve, Zfh1, and Grain, regulates the expression of Fas 2, amongst other adhesion molecules (Zarin et al., 2014). In particular, Fas 2 is

bioRxiv preprint doi: https://doi.org/10.1101/092486; this version posted December 8, 2016. The copyright holder for this preprint (which was not certified by peer review) is the author/funder, who has granted bioRxiv a license to display the preprint in perpetuity. It is made available under aCC-BY-ND 4.0 International license.

downregulated in aCC and RP2 (*puc* positive) neurons in *zfh1* mutants. The *zfh1* gene is a transcription factor containing two kruppel-like zinc-fingers and a homeodomain (Fortini, Lai et al., 1991). Zfh1 has been previously linked to JNK activity in the nervous system although their relationship is not clear. While in *Drosophila* Zfh1 blocks both JNK activation and activity in glia preventing apoptosis (Ohayon, Pattyn et al., 2009), in mice, JNK activity is downregulated in the hippocampus in *zfh1* (*Sip1*) mutants (Miquelajauregui, Van de Putte et al., 2007). We found that *zfh1* embryos display similar phenotypes to *puc*: defasciculation of Fas 2 connectives and failure of VNC condensation (Figure 7 and S7). Further, Fas 2 levels, as for *puc*, were downregulated for *zfh1*. Zfh1 (which is expressed in motor neurons (Layden, Odden et al., 2006) including most of those expressing *puc*) is partially downregulated in *puc* mutants (Figure 7 and S7).

Altogether, our data suggest that the activation of *puc* expression by JNK in early-specified pioneer neurons (aCC, pCC, RP2, dMP2 and VUMs) results in the downregulation of the pathway and an overall increase in Fas 2 levels (in part as a result of *zfh1* expression). A deficit in Fas 2 affects the fasciculation of the axons of primary neurons, leading to secondary bundling defects that result in a general reduction in spatial correlations across the whole axonal network of the neuropile. Failure to properly fasciculate eventually affects both the architectural organization and the tensional balance of the VNC, ultimately impeding its condensation (Figure 7).

bioRxiv preprint doi: https://doi.org/10.1101/092486; this version posted December 8, 2016. The copyright holder for this preprint (which was not certified by peer review) is the author/funder, who has granted bioRxiv a license to display the preprint in perpetuity. It is made available under aCC-BY-ND 4.0 International license.

REFERENCES

Adachi-Yamada T, Fujimura-Kamada K, Nishida Y, Matsumoto K (1999) Distortion of proximodistal information causes JNK-dependent apoptosis in Drosophila wing. Nature 400: 166-9

Arendt D, Tosches MA, Marlow H (2016) From nerve net to nerve ring, nerve cord and brain--evolution of the nervous system. Nature reviews Neuroscience 17: 61-72

Cajal SRy (1899) Textura del Sistema Nervioso del Hombre y de los Vertebrados trans. Nicolas Moya, Madrid, Spain

Chen BL, Hall DH, Chklovskii DB (2006) Wiring optimization can relate neuronal structure and function. Proceedings of the National Academy of Sciences USA 103: 4723-8

Chklovskii DB, Koulakov AA (2004) Maps in the brain: what can we learn from them? Annual review of neuroscience 27: 369-92

Davis RJ (2000) Signal transduction by the JNK group of MAP kinases. Cell 103: 239-52

Fortini ME, Lai ZC, Rubin GM (1991) The Drosophila zfh-1 and zfh-2 genes encode novel proteins containing both zinc-finger and homeodomain motifs. Mechanisms of development 34: 113-22

Franze K (2013) The mechanical control of nervous system development. Development 140: 3069-77

Fritsch M, Richter S (2010) The formation of the nervous system during larval development in Triops cancriformis (Bosc) (crustacea, Branchiopoda): An immunohistochemical survey. Journal of morphology 271: 1457-81

Harzsch S (2001) Neurogenesis in the crustacean ventral nerve cord: homology of neuronal stem cells in Malacostraca and Branchiopoda? Evolution & development 3: 154-69

Hsieh MH, Nguyen HT (2005) Molecular mechanism of apoptosis induced by mechanical forces. International review of cytology 245: 45-90

Ip YT, Davis RJ (1998) Signal transduction by the c-Jun N-terminal kinase (JNK)--from inflammation to development. Current opinion in cell biology 10: 205-19

Jacobs JR, Goodman CS (1989) Embryonic development of axon pathways in the Drosophila CNS. II. Behavior of pioneer growth cones. The Journal of neuroscience 9: 2412-22

bioRxiv preprint doi: https://doi.org/10.1101/092486; this version posted December 8, 2016. The copyright holder for this preprint (which was not certified by peer review) is the author/funder, who has granted bioRxiv a license to display the preprint in perpetuity. It is made available under aCC-BY-ND 4.0 International license.

Kuan CY, Yang DD, Samanta Roy DR, Davis RJ, Rakic P, Flavell RA (1999) The Jnk1 and Jnk2 protein kinases are required for regional specific apoptosis during early brain development. Neuron 22: 667-76

Landgraf M, Sanchez-Soriano N, Technau GM, Urban J, Prokop A (2003) Charting the Drosophila neuropile: a strategy for the standardised characterisation of genetically amenable neurites. Developmental biology 260: 207-25

Layden MJ, Odden JP, Schmid A, Garces A, Thor S, Doe CQ (2006) Zfh1, a somatic motor neuron transcription factor, regulates axon exit from the CNS. Developmental biology 291: 253-63

Leise EM (1990) Modular construction of nervous systems: a basic principle of design for invertebrates and vertebrates. Brain research reviews 15: 1-23

Lin DM, Fetter RD, Kopczynski C, Grenningloh G, Goodman CS (1994) Genetic analysis of Fasciclin II in Drosophila: defasciculation, refasciculation, and altered fasciculation. Neuron 13: 1055-69

Martin-Blanco E (1998) Regulatory control of signal transduction during morphogenesis in Drosophila. The International journal of developmental biology 42: 363-8

Martin-Blanco E, Gampel A, Ring J, Virdee K, Kirov N, Tolkovsky AM, Martinez-Arias A (1998) puckered encodes a phosphatase that mediates a feedback loop regulating JNK activity during dorsal closure in Drosophila. Genes & development 12: 557-70

Matheson T (2002) Invertebrate Nervous Systems. Encyclopedia of Life Sciences: 1-6

Miquelajauregui A, Van de Putte T, Polyakov A, Nityanandam A, Boppana S, Seuntjens E, Karabinos A, Higashi Y, Huylebroeck D, Tarabykin V (2007) Smad-interacting protein-1 (Zfhx1b) acts upstream of Wnt signaling in the mouse hippocampus and controls its formation. Proceedings of the National Academy of Sciences USA 104: 12919-24

Ohayon D, Pattyn A, Venteo S, Valmier J, Carroll P, Garces A (2009) Zfh1 promotes survival of a peripheral glia subtype by antagonizing a Jun N-terminal kinase-dependent apoptotic pathway. The EMBO journal 28: 3228-43

Qing Yu ZL, Chuanzi OuYang, Lingjun Li (2015) Biologically Active Peptides in Invertebrates: Discovery and Functional Studies. In Colloqium Series on neuropeptides, p 182. Morgan & Claypool Publishers

bioRxiv preprint doi: https://doi.org/10.1101/092486; this version posted December 8, 2016. The copyright holder for this preprint (which was not certified by peer review) is the author/funder, who has granted bioRxiv a license to display the preprint in perpetuity. It is made available under aCC-BY-ND 4.0 International license.

Redies C, Puelles L (2001) Modularity in vertebrate brain development and evolution. BioEssays 23: 1100-11

Sanchez-Soriano N, Tear G, Whitington P, Prokop A (2007) Drosophila as a genetic and cellular model for studies on axonal growth. Neural development 2: 9

Shklover J, Mishnaevski K, Levy-Adam F, Kurant E (2015) JNK pathway activation is able to synchronize neuronal death and glial phagocytosis in Drosophila. Cell death & disease 6: e1649

Siechen S, Yang S, Chiba A, Saif T (2009) Mechanical tension contributes to clustering of neurotransmitter vesicles at presynaptic terminals. Proceedings of the National Academy of Sciences USA 106: 12611-6

Sporns O, Betzel RF (2016) Modular Brain Networks. Annu Rev Psychol 67: 613-40

Srahna M, Leyssen M, Choi CM, Fradkin LG, Noordermeer JN, Hassan BA (2006) A signaling network for patterning of neuronal connectivity in the Drosophila brain. PLoS biology 4: e348

Technau GM (2008) Brain development in Drosophila melanogaster. Springer Science+Business Media, LLC - Landes Bioscience,

Tessier-Lavigne M, Goodman CS (1996) The molecular biology of axon guidance. Science 274: 1123-33

Van Essen DC (1997) A tension-based theory of morphogenesis and compact wiring in the central nervous system. Nature 385: 313-8

Waetzig V, Herdegen T (2004) Neurodegenerative and physiological actions of c-Jun N-terminal kinases in the mammalian brain. Neuroscience letters 361: 64-7

Zarin AA, Asadzadeh J, Hokamp K, McCartney D, Yang L, Bashaw GJ, Labrador JP (2014) A transcription factor network coordinates attraction, repulsion, and adhesion combinatorially to control motor axon pathway selection. Neuron 81: 1297-311

Zlatic M, Li F, Strigini M, Grueber W, Bate M (2009) Positional cues in the Drosophila nerve cord: semaphorins pattern the dorso-ventral axis. PLoS biology 7: e1000135

bioRxiv preprint doi: https://doi.org/10.1101/092486; this version posted December 8, 2016. The copyright holder for this preprint (which was not certified by peer review) is the author/funder, who has granted bioRxiv a license to display the preprint in perpetuity. It is made available under aCC-BY-ND 4.0 International license.

ACKNOWLEDGMENTS

We are extremely grateful to all colleagues that have provided us materials, training and guidance throughout this work as well as for commenting on the manuscript. Amongst them we like to specially thank Matthias Landgraf, Chris Doe, Andreas Prokop, Natalia Sanchez-Soriano, Stefan Richter, Martin Fritsch, Marta Zlatic, Albert Cardona, Irene Miguel-Aliaga and Ruth Lehmann. We also have to thank our colleagues at the Parc Cientific de Barcelona, the Mechanobiology Institute of Singapore and the Fleming Institute of Athens for their constant encouragement and support.

bioRxiv preprint doi: https://doi.org/10.1101/092486; this version posted December 8, 2016. The copyright holder for this preprint (which was not certified by peer review) is the author/funder, who has granted bioRxiv a license to display the preprint in perpetuity. It is made available under aCC-BY-ND 4.0 International license.

FIGURES

Figure 1

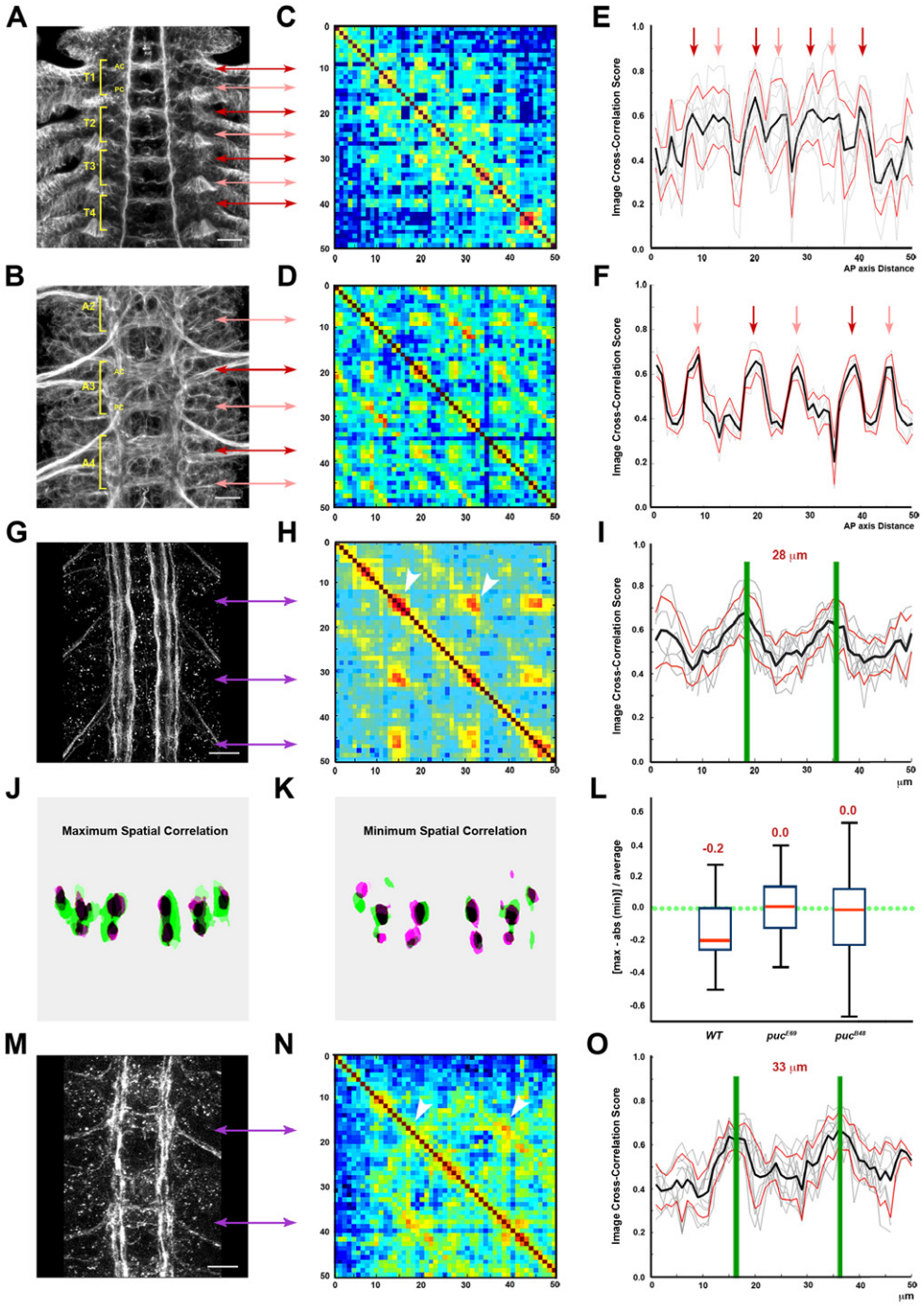

bioRxiv preprint doi: https://doi.org/10.1101/092486; this version posted December 8, 2016. The copyright holder for this preprint (which was not certified by peer review) is the author/funder, who has granted bioRxiv a license to display the preprint in perpetuity. It is made available under aCC-BY-ND 4.0 International license.

Figure 1. Conservation of the Structural Architecture of the Ventral Nerve Cord (VNC) in Arthropods

A) Acetylated α-Tubulin immunoreactivity. Maximum projection of a ventral view of the first four thoracic neuromeres (T1 to T4) of the VNC of a larva II (LII) of *Triops cancriformis* (Notostraca) (original dataset by Martin Fritsch, University of Rostock). The nervous system in LII features a developing brain where neuromeres are connected via two connectives proceeding in a posterior direction. In each neuronal segment the primordial ganglia are connected by an anterior (AC) and a posterior commissure (PC). Scale Bar is 20 μm.

B) Acetylated α-Tubulin immunoreactivity. Maximum projection of a ventral view of three abdominal segments (A2 to A4) of the VNC of a 16-stage embryo of *Drosophila*. Anterior (AC) and posterior commissures (PC) are indicated. See Movie S1. Scale Bar is 10 μm.

C) Self cross-correlation matrix of the Z sections of the image in **A** (dividing the full length of the image in 50 bins) along the A/P axis. The color-coded representation, in all figures from now on, nicely shows the correlation level for each possible comparison at each position along the A/P axis and allows the comparison with the original morphological data. In this way it was possible to identify an oscillatory pattern of hot spots (nodes - two per segment - red and pink double headed arrows) of high correlation.

D) Self cross-correlation matrix for **B**. In *Drosophila*, two robust nodes are also evident at each segment.

E) Image cross-correlation score along the A/P axis for **C**. In all figures from now on, individual profiles are plotted in gray, with the Mean (black) and ± Standard Deviation (red) shown. Red and pink arrows point to the dual-oscillatory cross-correlation maxima.

F) Image cross-correlation score along the A/P axis for **D**. Dual oscillation is sustained in *Drosophila*.

G) Maximum projection of the VNC of a *Drosophila* 16-stage *wt* embryo stained with Fas 2. See Movie S2. Scale Bar is 10 μm.

H) Self cross-correlation matrix of the Z sections of the image in **G**. One conspicuous node of robust correlation per segment is detected (white arrowheads).

I) Image cross-correlation score along the A/P axis for **H**. The cross-correlation profile shows that segmental Fas 2 nodes fell 17 μm apart in *wt* animals and that the internodal maximum

bioRxiv preprint doi: https://doi.org/10.1101/092486; this version posted December 8, 2016. The copyright holder for this preprint (which was not certified by peer review) is the author/funder, who has granted bioRxiv a license to display the preprint in perpetuity. It is made available under aCC-BY-ND 4.0 International license.

noise/minimum correlation maps 6 μm posterior to the node.

J) Z sections at two different maximal (green and magenta) correlation positions (from **G**) showing coalescence of Fas 2 connectives at the nodes.

K) Z sections at two different minimal (green and magenta) correlation positions (from **G**) showing dispersion and stochastic distribution associated to internodal noise.

L) Box plots of the differences vs. the mean for the variable r = [max (grad) - abs (min (grad))] / [(max (grad) + abs (min (grad))) / 2] between datasets for *wt*, puc^{E69} and puc^{B48} individuals. The median from *wt* was clearly less than zero with a 95% confidence interval. For the mutants this was lost, with the values not distinguishable from zero. The bias in *wt* values indicates that the decay in robustness from nodes in the posterior direction is more pronounced than its recovery towards subsequent nodes. This behavior is abolished for puc^{E69} and puc^{B48}.

M) Equivalent image to **G** for a puc^{E69} homozygous embryo. Note the defasciculation and collapse of the longitudinal connectives, specially the most lateral ones. See Movie S3. Scale Bar is 10 μm.

N) Self cross-correlation matrix of the Z sections of the image in **J**. In puc^{E69} mutants, while correlation matrices are noisier, a single node per segment can still be observed. One conspicuous node of robust correlation per segment was detected (white arrowheads).

O) Image cross-correlation score along the A/P axis for **K**. Segmental Fas 2 nodes spread 20 μm away in puc^{E69} and the internodal minima gets diffuse.

bioRxiv preprint doi: https://doi.org/10.1101/092486; this version posted December 8, 2016. The copyright holder for this preprint (which was not certified by peer review) is the author/funder, who has granted bioRxiv a license to display the preprint in perpetuity. It is made available under aCC-BY-ND 4.0 International license.

Figure 2

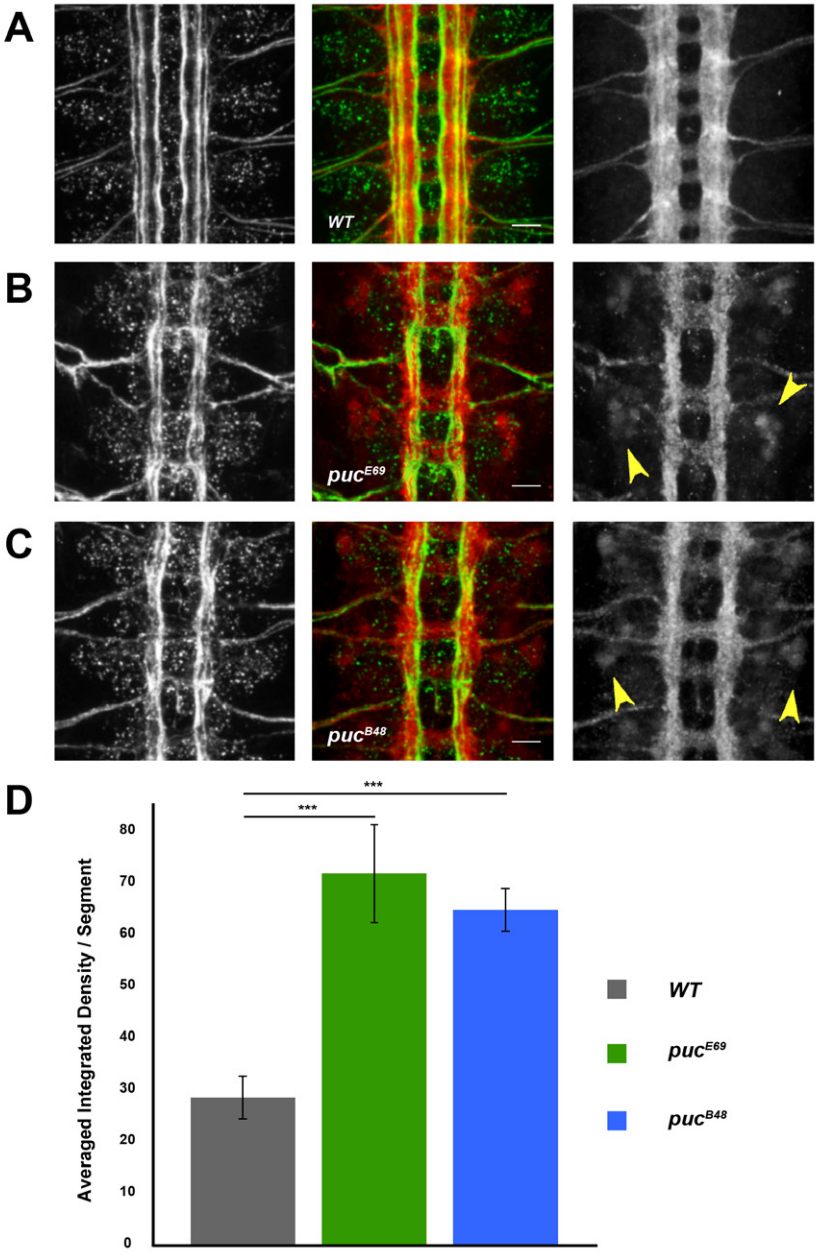

Figure 2. JNK activity in *puc* mutants

A) Single (left and right) and combined (centre) channels highlighting the expression of Fas 2 (left - green) and anti-P-JNK (right- red) of a stage 17 *wt* embryo. Scale Bar is 10 µm.

B) Equivalent as A for a stage 17 puc^{E69} embryo. Scale Bar is 10 µm.

C) Equivalent as A for a stage 17 puc^{B48} embryo. Scale Bar is 10 µm.

bioRxiv preprint doi: https://doi.org/10.1101/092486; this version posted December 8, 2016. The copyright holder for this preprint (which was not certified by peer review) is the author/funder, who has granted bioRxiv a license to display the preprint in perpetuity. It is made available under aCC-BY-ND 4.0 International license.

In mutant embryos (**B** and **C**) a significant fraction of the P-JNK signal remained in or around cell bodies (yellow arrowheads) and is not strictly found as in *wt* only in axons.

D) Graph displaying the averaged Integrated Density per segment for the P-JNK signal. Statistically significant differences in P-JNK levels ($p < 0.001$) were detected between the *wt* and both mutant conditions.

Figure 3

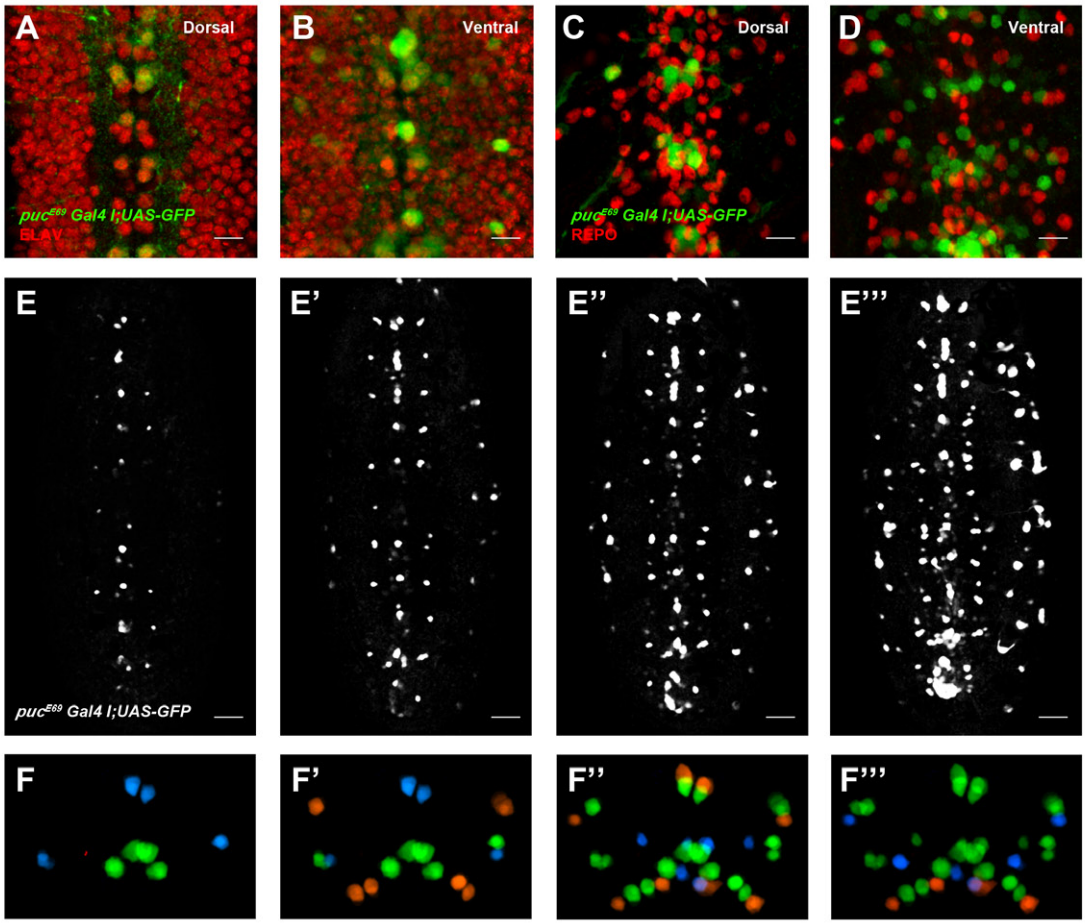

Figure 3. JNK signaling is dynamically regulated during development

A to **D)** Dorsal and ventral sections highlighting the expression of *puc* (green) in the VNC of stage 17 UAS-GFP; *puc*^{E69}*I*-Gal4 embryo double-stained for the pan-neuronal marker Elav (**A** and **B** - red) or the glial marker Repo (**C** and **D** - red). *puc* is expressed in a subset of neurons in each segments but not in glia. Scale Bar is 10 µm.

E to **E''')** four different snapshots from Movie S4 at the indicated time points from the UAS-

bioRxiv preprint doi: https://doi.org/10.1101/092486; this version posted December 8, 2016. The copyright holder for this preprint (which was not certified by peer review) is the author/funder, who has granted bioRxiv a license to display the preprint in perpetuity. It is made available under aCC-BY-ND 4.0 International license.

GFP; *puc*^{E69}*I*-Gal4 viable line. *puc* expression can be observed from early stage 13 in a few neurons at midline. As development progressed, more and more neurons express *puc*. Scale Bar is 10 µm.

F to **F'''**) Diagram displaying the cumulative expression of *puc* at the same time points as in **E** to **E'''**. A minimum consensus of 19 neurons per hemisegment was defined. At each time point the intensity (defined by visual inspection) was displayed as low (red), medium (blue) and high (green) (see also Movie S5).

Figure 4

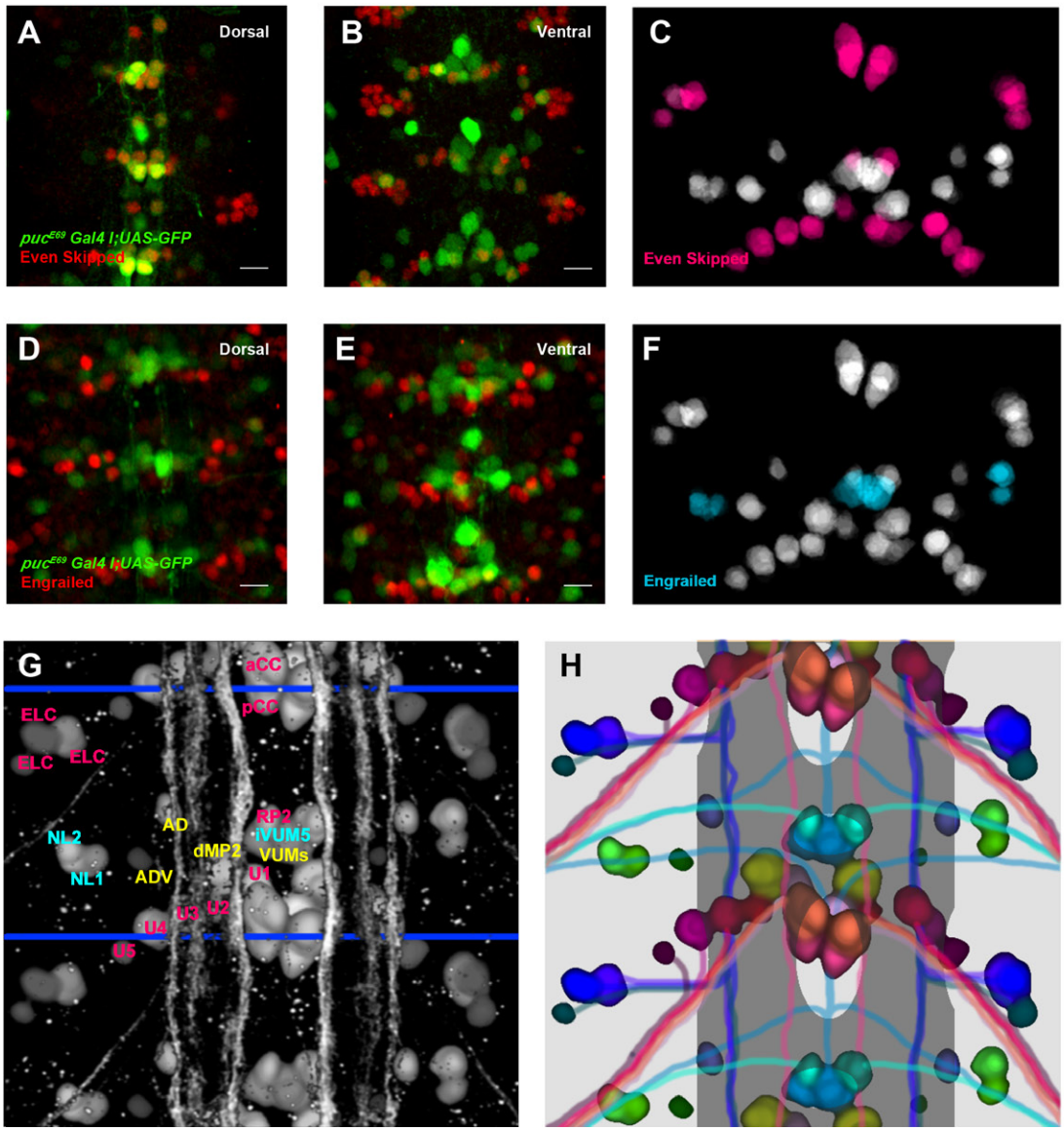

bioRxiv preprint doi: https://doi.org/10.1101/092486; this version posted December 8, 2016. The copyright holder for this preprint (which was not certified by peer review) is the author/funder, who has granted bioRxiv a license to display the preprint in perpetuity. It is made available under aCC-BY-ND 4.0 International license.

Figure 4. Identities of *puc*-expressing neurons

A and **B)** Dorsal and ventral sections highlighting the expression of *puc* (green) in the VNC of stage 17 UAS-GFP; $puc^{E69}I$-Gal4 embryo double-stained for Even-Skipped (red). Scale Bar is 10 µm.

C) Diagram indicating those *puc* expressing cells also expressing Even-Skipped [magenta - aCC, pCC, RP2, U1-U3 (plus weak/variable expression in U4-U5) and 3 out of the 8 to 10 ELC interneurons].

D and **E)** Dorsal and ventral sections highlighting the expression of *puc* (green) in the VNC of stage 17 UAS-GFP; $puc^{E69}I$-Gal4 embryo double-stained for Engrailed (red). Scale Bar is 10 µm.

F) Diagram indicating those *puc* expressing cells also expressing Engrailed (cyan - NL1, NL2, and iVUM5 neurons).

G) Composition summarizing the expression of *puc* in the CNS [*puc* expressing cells in the VNC at stage 16 including those identified by coexpressing Even-skipped (magenta) or Engrailed (cyan) plus those putatively identified by morphological and positional criteria (yellow - AD, ADV, dMP2 and 2 VUM En-negative motor neurons)]. To facilitate understanding, a scaled Fas 2 expression image from an embryo of the same stage was overimposed to the diagram. Positions of the robustness nodes are highlighted as dark blue lines.

H) Diagram representing the whole set of *puc* expressing cells (compare to G) and their expected axonal contributions to connectives and exiting nerves (each individual cell carried a single color-code). This diagram was over-imposed over a grey mask covering the scaled width and shape of the VNC.

bioRxiv preprint doi: https://doi.org/10.1101/092486; this version posted December 8, 2016. The copyright holder for this preprint (which was not certified by peer review) is the author/funder, who has granted bioRxiv a license to display the preprint in perpetuity. It is made available under aCC-BY-ND 4.0 International license.

Figure 5

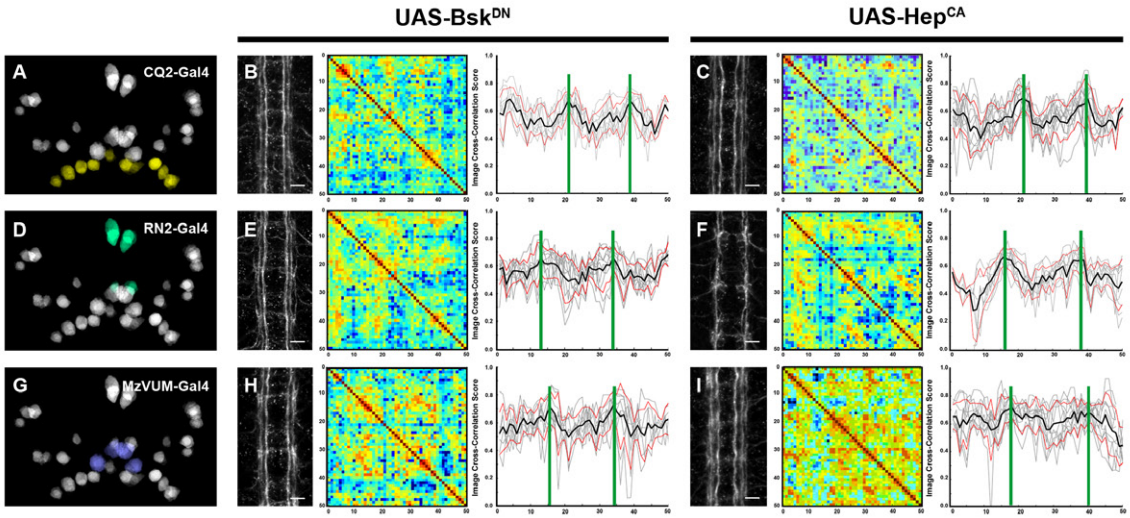

Figure 5. Targeted activation and inhibition of the JNK pathway in the VNC

A) Cartoon representing the full set of *puc* expressing neurons per segment in the VNC highlighting the cells expressing CQ2-Gal4 (yellow).

B and **C)** From left to right, pattern of Fas 2 expression, self cross-correlation matrix and image cross-correlation profiles for VNCs of 16-stage embryos upon expression of UAS-Bsk^{DN} **(B)** and UAS-Hep^{CA} **(C)** transgenes under the control of the CQ2-Gal4 respectively inhibiting and hyperactivating JNK activity in the U motoneurons. None of these conditions result in noticeable defects. Scale Bar is 10 µm.

D) Cartoon highlighting the *puc* positive cells expressing RN2T-Gal4 (turquoise).

E and **F)** As **B** and **C** but employing RN2T-Gal4 for interfering in JNK activity in the aCC, pCC and RP2 cells. Affecting JNK activity levels in aCC, pCC and RP2 cells affect connectives defasciculation, nodes profiles and VNC condensation. Scale Bar is 10 µm.

G) Cartoon highlighting the *puc* positive neurons expressing MzVum-Gal4 (purple).

H and **I)** As **B** and **C** but employing MzVum-Gal4 for interfering in JNK activity in the VUM neurons. Affecting JNK activity levels in VUMs also affects defasciculation, profiles and condensation. Scale Bar is 10 µm.

bioRxiv preprint doi: https://doi.org/10.1101/092486; this version posted December 8, 2016. The copyright holder for this preprint (which was not certified by peer review) is the author/funder, who has granted bioRxiv a license to display the preprint in perpetuity. It is made available under aCC-BY-ND 4.0 International license.

Figure 6

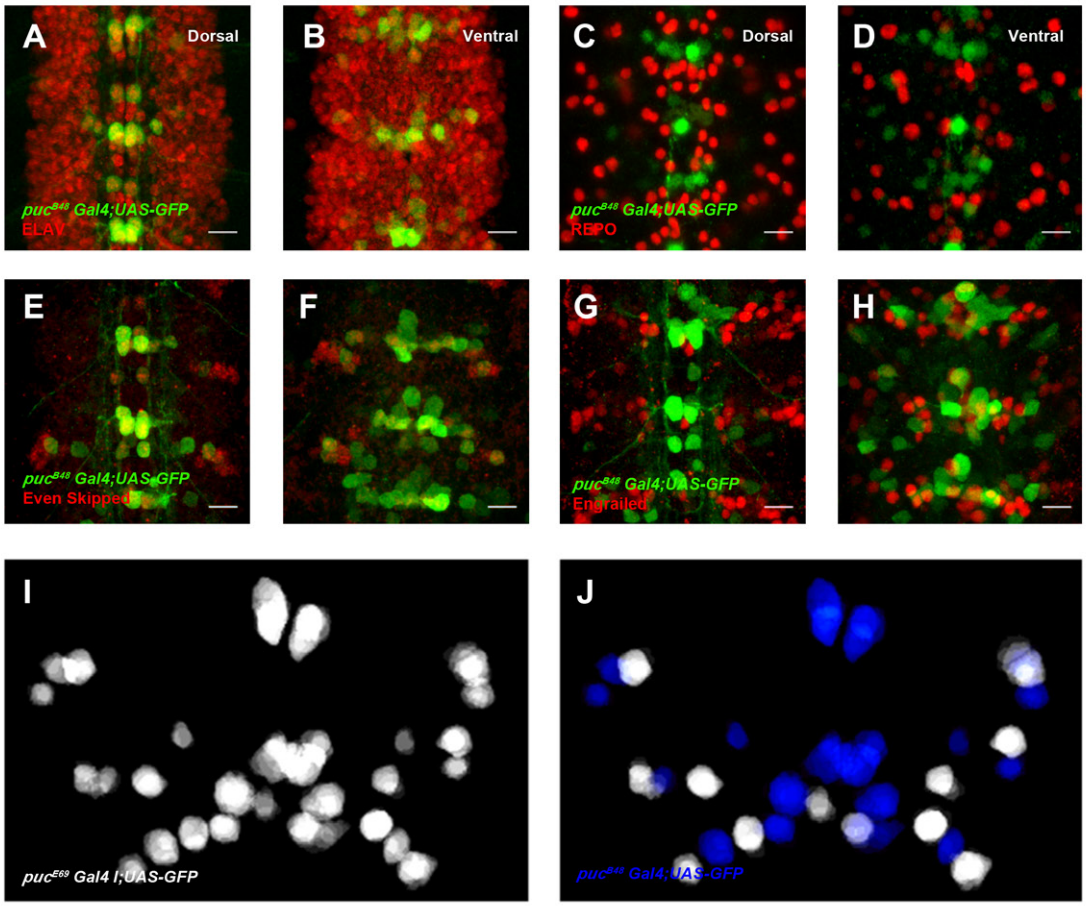

Figure 6. Fasciclin 2 expression is reduced in *puc* mutants

A) *wt*, **B)** puc^{E69} and **C)** puc^{B48} stage 16 embryos Fas 2 immunoreactivity. Maximum projection of ventral views across three VNC abdominal segments. Overlaid squares represent the fixed area ROIs used for measuring the Average Integrated Density of Fas 2 signal, either at the node (red) or at the internode (yellow) positions. Scale Bar is 10 µm.

D) Quantification of the Average Integrated Density of Fas 2 signal at node and internode positions as indicated. Statistically significant differences in Fas 2 levels ($p < 0.0001$) were detected between *wt* and *puc* embryos, both at the node and internode positions.

E) Immunodetection of Fas 2 in extracts from stage 16 *puc* embryos. Extracts of balanced siblings were used as controls. In control extracts, the antibody against Fas 2 detected a strong band at 95 kD (red arrow), the intensity of which was reduced by half in extracts from *puc* homozygous embryos. Detection of actin (42 kD) served as loading control for the quantification

bioRxiv preprint doi: https://doi.org/10.1101/092486; this version posted December 8, 2016. The copyright holder for this preprint (which was not certified by peer review) is the author/funder, who has granted bioRxiv a license to display the preprint in perpetuity. It is made available under aCC-BY-ND 4.0 International license.

of the Fas 2 signal. The graph represents the averaged Fas 2 band intensities normalized with respect to actin.

Figure 7

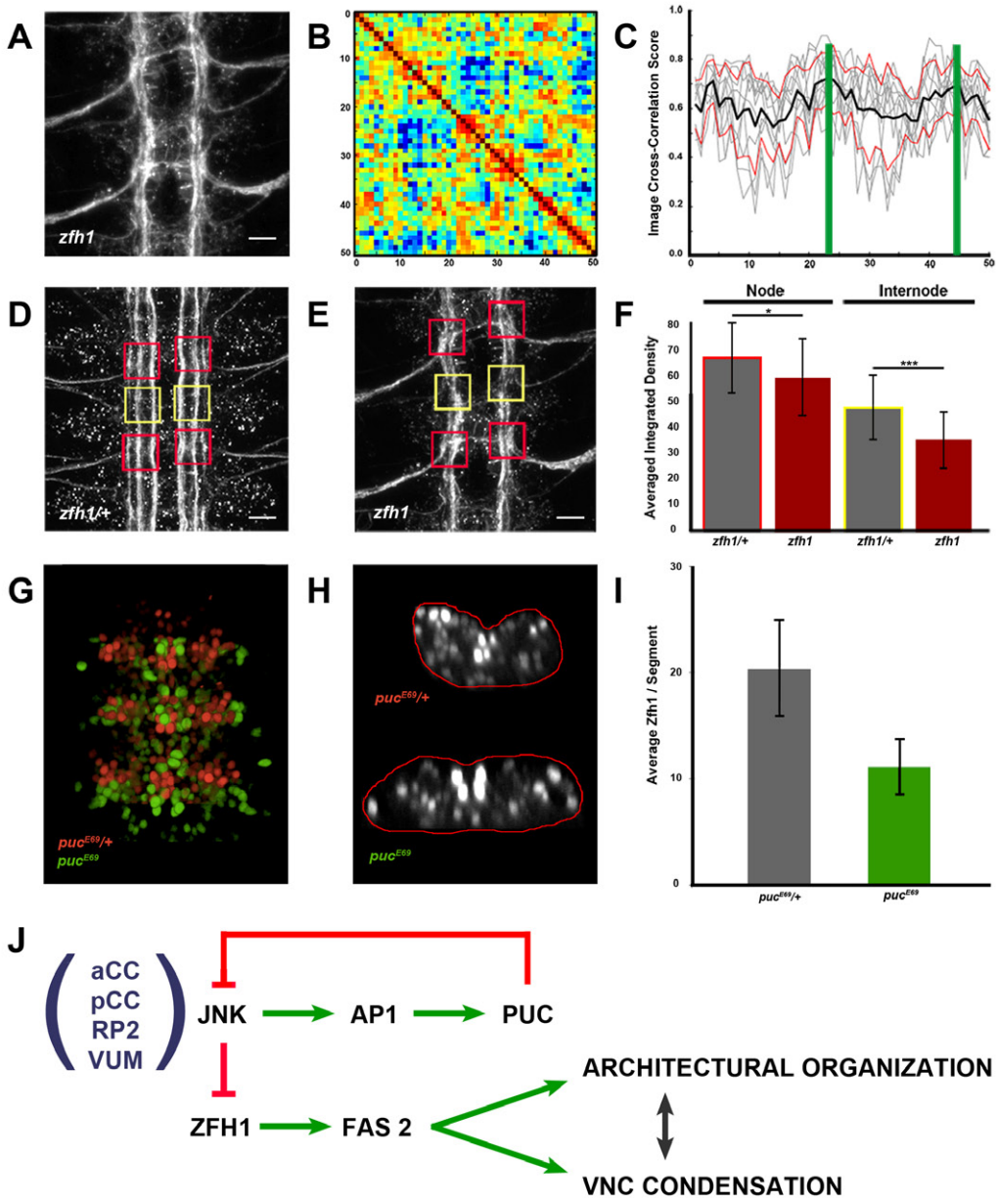

Figure 7. *zfh1* mutants display low Fasciclin 2 expression and show intersegmental correlation defects

A) Pattern of Fas 2 expression for VNCs of 16-stage *zfh1* embryos. Scale Bar is 10 µm.

bioRxiv preprint doi: https://doi.org/10.1101/092486; this version posted December 8, 2016. The copyright holder for this preprint (which was not certified by peer review) is the author/funder, who has granted bioRxiv a license to display the preprint in perpetuity. It is made available under aCC-BY-ND 4.0 International license.

B) Self cross-correlation matrix from **B**.

C) Image cross-correlation profiles. Longitudinal connectives defasciculate and, although segmental nodes were still present, segments did not condense and the robustness profile was distorted.

D) Fas 2 immunoreactivity for *zfh1* heterozygous stage 16 embryos. Maximum projections of ventral views across three VNC abdominal segments are shown. Overlaid squares represent the fixed area ROIs used for measuring the Fas 2 signal, either at the node (red) or at the internode (yellow) positions. Scale Bar is 10 µm.

E) Fas 2 immunoreactivity for *zfh1* homozygous stage 16 embryos. Maximum projections of ventral views as for **D**. ROIs as for **D**. Scale Bar is 10 µm.

F) Quantification of the Average Integrated Density of Fas 2 signal at node and internode positions. Statistically significant differences in Fas 2 levels ($p < 0.0001$) were detected between heterozygous and homozygous *zfh1* embryos, both at the node (red vs. grey with red rim) and internode (red vs. grey with yellow rim) positions.

G) Overimposed scaled 3D images of Zfh1 expressing cells of three sequential segments of the VNCs of heterozygous (red) and homozygous (green) puc^{E69} embryos. Note the lack of condensation and widening of the homozygous puc^{E69} VNC. See Movie S6

H) Outlined (red) cross sections of puc^{E69}/+ and puc^{E69} VNCs at the level of the anterior commissures. Subsets of dorsal and ventral cells lose Zfh1 in homozygous animals. Note the differential shape (flattening and widening) of the puc^{E69} VNC

I) Graph displaying the averaged Integrated Density for the Zfh1 signal per segment of heterozygous (grey) and homozygous (green) puc^{E69} embryos.

J) Regulatory network modulating VNC architectural organization and condensation. Precise JNK activity levels in early-specified neurons (at least aCC, pCC, RP2 and VUMs) are regulated by a negative feedback loop mediated by Puc. Excessive JNK activity in *puc* mutants would lead to a general downregulation of Fas 2 (in part as a consequence of inhibiting Zfh1 expression) and the disorganization of the structural backbone of the VNC and its condensation failure.

bioRxiv preprint doi: https://doi.org/10.1101/092486; this version posted December 8, 2016. The copyright holder for this preprint (which was not certified by peer review) is the author/funder, who has granted bioRxiv a license to display the preprint in perpetuity. It is made available under aCC-BY-ND 4.0 International license.

SUPPLEMENTAL EXPERIMENTAL PROCEDURES

Drosophila strains

The following stocks were used:

w; *puc*^{E69}*LacZ/TM3, twi-GFP, w; puc*^{B48}*LacZ/ TM3, twi-GFP* (Martin-Blanco, Gampel et al., 1998)

w; UAS-GFP; *puc*^{E69}*I*–Gal4/TM6B, w; UAS-GFP; *puc*^{B48}–Gal4/TM6B (Pastor-Pareja, Grawe et al., 2004)

w[1118]P{w[+mC]=UAS-bsk.DN}2 (BDSC #6409)

w[*];P{w[+mC]=UAS-Hep.Act}2 (BDSC #9306)

P{GawB}elav[C155] (BDSC #6923)

*w[*]; P{w[+mC]=eve-GAL4.RN2}P,P{w[+mC]=UAS-mCD8::GFP.L}LL5 (*Dr. Irene Miguel-Aliaga)

y*[1] w[*];P{w[+mC]=CQ2-GAL4}O, P{w[+mC]=UAS-mCD8::GFP.L}LL6* (BDSC #7465)

*w[*] P{w[+mW.hs]=GawB}MzVUM; P{y[+t7.7] w[+mC] = 10xUAS-IVS-mCD8::GFP}attP40 (*Dr. Irene Miguel-Aliaga)

G3130 P[hs,neo,ry+,FRT82B]ca, zfh1 75, 26 / TM3 (Dr. Ruth Lehmann)

In all cases, unless otherwise stated, embryos of the *w1118* strain served as controls.

Immunohistochemistry

Immunostaining of flat-prepped stage 16 *Drosophila* embryos was performed using the following primary antibodies: mouse anti-Acetylated α-Tubulin (1:1500, Sigma T6793), mouse anti-Fas 2 (1:100, clone 1D4, DHSB), mouse anti-axons CNS (1:100, BP 102, DHSB), mouse anti-Futsch (1:1000, 22c10, DHSB), rabbit anti-phospho-JNK (Thr^{183} / Tyr^{185}) (1:100, Cell Signaling #9251), rabbit anti-Dcp-1 (Asp216) (1:100, Cell Signaling #9578), rabbit anti-GFP tag polyclonal (1:600, Thermo Fisher Scientific), rat anti-Elav (1:1000, clone 7E8A10, DHSB), mouse anti-Repo (1:100, clone 8D12 DHSB), mouse anti-Even-skipped (1:100, clone 3C10, DHSB), mouse anti-Engrailed (1:100, clone 4D9, DHSB) and rabbit anti-Zfh1 (1:2000, from Dr. Ruth Lehmann).

bioRxiv preprint doi: https://doi.org/10.1101/092486; this version posted December 8, 2016. The copyright holder for this preprint (which was not certified by peer review) is the author/funder, who has granted bioRxiv a license to display the preprint in perpetuity. It is made available under aCC-BY-ND 4.0 International license.

The secondary antibodies used for detection were: Goat anti-Rabbit IgG (H+L), Alexa Fluor 488 conjugate (A-11008), Goat anti-Rabbit IgG (H+L) Alexa Fluor 555 conjugate (A-21428), Goat anti-Mouse IgG (H+L) Alexa Fluor 488 conjugate (A-11001), Goat anti-Mouse IgG (H+L) Alexa Fluor 555 conjugate (A-21422) and Goat anti-Rat IgG (H+L) Alexa Fluor 555 conjugate (A-21434). All secondary antibodies were used in a dilution of 1:600 and were from Invitrogen.

Sample preparations for immunodetection and image acquisition

Drosophila embryo dissections for generating flat preparations were performed according to (Landgraf, Bossing et al., 1997). Briefly, flies maintained in apple juice-agar plates at 25ºC were synchronized by repetitive changes of the juice-agar plate, with a time interval of 1.5h. All embryos laid within this time window were aged for approximately 22 hours at 18ºC, or until reaching mid-stage 16 (3-part gut stage). At this point embryos were dechorionated with bleach for 1 min, poured into a mesh and rinsed extensively with water. For dissection, embryos were transferred with forceps on the surface of a small piece of double sided tape, adhered on one of the sides of a poly-L-Lysine coated coverslip. After orienting the embryos dorsal side up and posterior end towards the center of the coverslip, the coverslip was flooded with saline (0.075 M Phosphate Buffer, pH 7.2). Using a pulled glass needle the embryos were manually de-vitellinized and dragged to the center of the coverslip, where they were attached to the coated glass with their ventral side down. An incision on the dorsal side of the embryo was performed using the glass needle from the anterior to the posterior end of the embryo. The gut was removed by mouth suction and blowing stream of saline was used to flatten their lateral epidermis. Tissue fixation was done with 3.7 % formaldehyde in saline for 10 minutes at room temperature. After this point standard immuno-staining procedures were followed.

In the single case (Fig. S2) where whole mount embryos were immunostained, embryo fixation and de-vitalinization was done according to (Patel, 1994). Both whole mount and flat-prepped immunostained embryos were mounted in Vectashield anti-fading medium (Vector Laboratories, USA).

Image acquisition was performed on Zeiss LSM 700 inverted confocal microscope, using a 63 x oil objective lens (NA 1.4). Z-stacks spanning the whole VNC thickness were acquired applying

bioRxiv preprint doi: https://doi.org/10.1101/092486; this version posted December 8, 2016. The copyright holder for this preprint (which was not certified by peer review) is the author/funder, who has granted bioRxiv a license to display the preprint in perpetuity. It is made available under aCC-BY-ND 4.0 International license.

optimal, with respect to pinhole diameter, sectioning with a step size that varied between 0.2 – 0.6 μm. Image processing was performed with Fiji (Schindelin, Arganda-Carreras et al., 2012).

Western Blotting

Dechorionated stage 16 embryos of the *puc*^{E69}*LacZ / TM3, twi-GFP* and *puc*^{B48}*LacZ / TM3, twi-GFP* lines were used for generating whole embryo extracts for western blot analysis. In detail, homozygous embryos were separated from their balanced siblings under a fluorescent dissecting scope based on the *twi-GFP* expression. Approximately 100 embryos of each type were fully homogenized in 100 μL of iced cold RIPA buffer, supplemented with Protease Inhibitors (Protease Inhibitor Cocktail Tablets, Roche Life Sciences). Subsequently, the extracts were centrifuged at 3500 g for 15 minute at 4ºC and the supernatants were collected. Total protein concentration in the lysates was determined by Bradford assay (Bio-Rad) and 30 μg of sample were analyzed in a 10 % SDS-PAGE. Proteins were blotted on Protran nitrocellulose membrane (Whatman) while the antibodies employed were: anti-Fas 2 (1:1000, clone 1D4, DSHB) and Pan-actin (1:1000, Cell Signaling). The ECL Plus chemiluminescent substrate (Pierce, Thermo Fisher Scientific) was used for antibody detection. Western Blot signal quantification was performed with Fiji by measuring the average density of each band.

Live imaging

Dechorionated stage 14 embryos were glued ventral side down on a MatTek glass bottom dish and they were covered with S100 Halocarbon Oil (Merck) to avoid desiccation. Image acquisition was performed on Zeiss LSM 700 inverted confocal microscope, using a 25 x oil objective lens (NA 0.8). Z-stacks spanning the whole VNC thickness and with a 2 μm step size were acquired every 6 minutes for a total of 8 hours. Processing of time-lapse data was done with Fiji (Schindelin et al., 2012).

Image analysis

Image analysis and quantification of fluorescence intensity were performed using Fiji (Schindelin et al., 2012). In immunostainings where quantification of the fluorescent intensity

bioRxiv preprint doi: https://doi.org/10.1101/092486; this version posted December 8, 2016. The copyright holder for this preprint (which was not certified by peer review) is the author/funder, who has granted bioRxiv a license to display the preprint in perpetuity. It is made available under aCC-BY-ND 4.0 International license.

was required, extra care was taken so that the same antibody batch was used for staining embryos of different genotypes, while identical confocal acquisition settings were applied.

For calculating the average integrated density of Fas 2 signal in an image, regions of interest (ROIs) of fixed size were measured at the nodes and internodes positions. Average Integrated Density values obtained by measuring ROIs in several animals (n stated in Figure legends) were then pooled for calculating the mean value as well as standard deviations. For those cases where the quantification of integrated density was performed on a segment basis, the measured values represent the raw integrated density, since the area measured slightly varies in between animals.

Statistical analysis

All statistical analyses were performed using GraphPad Software (GraphPad Software Inc., La Jolla, CA, USA). In all cases one sample t test was performed and probability values $p<0.05$ were considered as significant.

Data analysis

Images were scaled to be isotropic in all axes. Deconvolution was found to not significantly improve the image correlation. Viewed along the antero-posterior axis, images were cropped to include only the VNC, and then the VNC was differentiated into 50 bins, corresponding to 1,65 μm length each. Within each bin, a maximum intensity projection was performed along the included (typically eleven) planes. The Matlab function *imregister* was then used to perform the image registration for both inter- and intra- embryo correlations. The optimizer for *imregister* was defined with multimodal metric, tolerance of 10^{-6} and 500 iterations. Before image registration, the center of mass of the two images was aligned so to maximize image overlap. The code was run on a PC with 128 Gb memory and in the most demanding case (full embryo correlation: 50 x 50 = 2500 correlations) took around one hour per sample.

To create the image correlation traces, the regions of high correlation (e.g. as identified by arrows in Fig. 1) were manually identified and then plotted considering the mean correlation along ± 1 row in the correlation matrices. The diagonal values were ignored. Traces were offset along AP axis to ensure maximum overlap of peaks in the region 25-57 μm to aid comparison between different datasets. In all figures, individual profiles are plotted in gray, with the mean

bioRxiv preprint doi: https://doi.org/10.1101/092486; this version posted December 8, 2016. The copyright holder for this preprint (which was not certified by peer review) is the author/funder, who has granted bioRxiv a license to display the preprint in perpetuity. It is made available under aCC-BY-ND 4.0 International license.

(black) and ± 1 standard deviation (red) shown. For each maximum in the spatial correlation profile, and a subset of data was sliced that lay between the two minima at either side. Then, we created *in silico* data from the real experimental data points - i.e. each *in silico* data point was drawn from a distribution defined by the mean and standard deviation in the samples. We determined the best linear fit to each *in silico* data set and repeated 500 times to find the average gradient fit. This was a robust way to find the steepness as it accounts for experimental noise. To compare between datasets, we defined the variable

r = (max(gradient) - abs(min(gradient))) / [(max(gradient)+abs(min(gradient)))/2]

i.e. the difference / mean.

bioRxiv preprint doi: https://doi.org/10.1101/092486; this version posted December 8, 2016. The copyright holder for this preprint (which was not certified by peer review) is the author/funder, who has granted bioRxiv a license to display the preprint in perpetuity. It is made available under aCC-BY-ND 4.0 International license.

SUPPLEMENTAL FIGURES

Figure S1

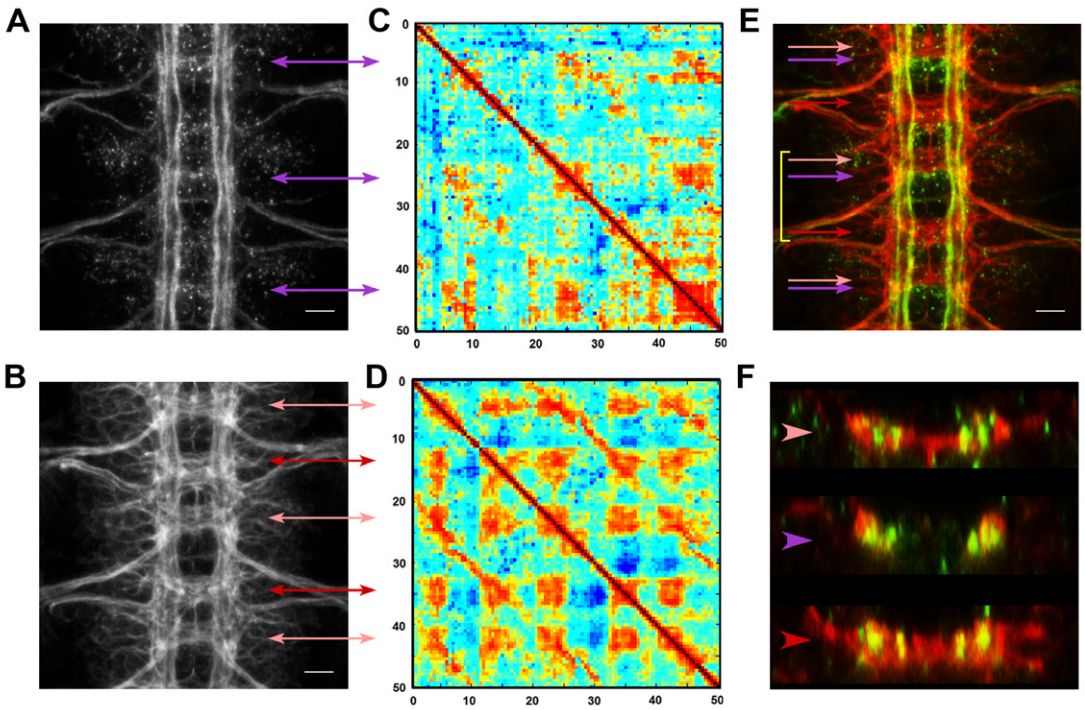

Figure S1. Structural organization of the *Drosophila* VNC

A) Fas 2 immunoreactivity. Maximum projection of a ventral view of three abdominal segments of the VNC of a 16-stage *Drosophila* embryo . Fas 2 axons organize in several longitudinal connectives grouped in three main medio-lateral positions. Fas 2 also decorates exiting axons.

B) Same embryo as in A double stained for Acetylated α-Tubulin. The whole set of axonal projections in the VNC are highlighted.

C) Self cross-correlation matrix of the Z sections of the image in **A**. Three main conspicuous nodes of robust correlation (one per segment) are detected (purple double-headed arrows).

D) Self cross-correlation matrix for **B**. Two robust nodes are evident at each segment (red and pink double-headed arrows).

E) Overimposed images **A** and **B** (Fas 2 - green and Acetylated α-Tubulin - red). Color coded arrows point to the Acetylated α-Tubulin anterior (pink) and posterior (red) commissure nodes

bioRxiv preprint doi: https://doi.org/10.1101/092486; this version posted December 8, 2016. The copyright holder for this preprint (which was not certified by peer review) is the author/funder, who has granted bioRxiv a license to display the preprint in perpetuity. It is made available under aCC-BY-ND 4.0 International license.

and to the Fas 2 nodes (purple). Note that these ones are offset from the pink ones and shifted posteriorly. Scale Bar is 10 µm.

F) Z sections at the level of the pink, purple and red nodes for a single segment (in brackets in **E**). While Acetylated α-Tubulin signal (red) is prominently grouped at the levels of the pink and red nodes, Fas 2 staining (green) shows longitudinal connectives grouping together at each hemisegment at the level of the purple node. At the positions of the pink and red commissure nodes, Fas 2 connectives are fairly dispersed.

Figure S2

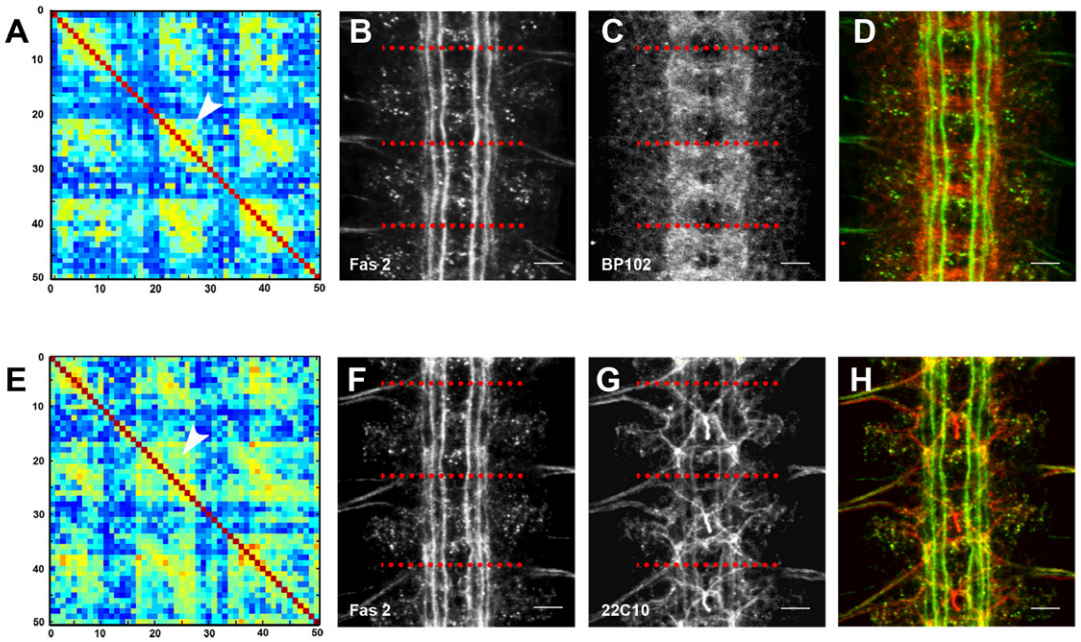

Figure S2. Fine localization of robustness nodes

A) Self cross-correlation matrix of the Z sections of the image in **B**. A conspicuous node of robust correlation is highlighted (white arrowhead).

B to **D)** Images for Fas 2 (**B** - green in **D**), BP102 (**C** - red in **D**) and their superimposed image (**D**) of a double-stained 16 stage *wt* embryo. Discontinued red lines indicate the localization of the robustness nodes in relation to the VNC pattern. Scale Bar is 10 µm.

E) Self cross-correlation matrix of the Z sections of the image in **F**. A conspicuous node of

bioRxiv preprint doi: https://doi.org/10.1101/092486; this version posted December 8, 2016. The copyright holder for this preprint (which was not certified by peer review) is the author/funder, who has granted bioRxiv a license to display the preprint in perpetuity. It is made available under aCC-BY-ND 4.0 International license.

robust correlation is highlighted (white arrowhead).

F to **H)** Images for Fas 2 (**F** - green in **H**), 22C10 (**G** - red in **H**) and their superimposed image (H) of a double-stained 16 stage *wt* embryo. Discontinued red lines indicate the localization of the robustness nodes in relation to the VNC pattern. Scale Bar is 10 µm.

Figure S3

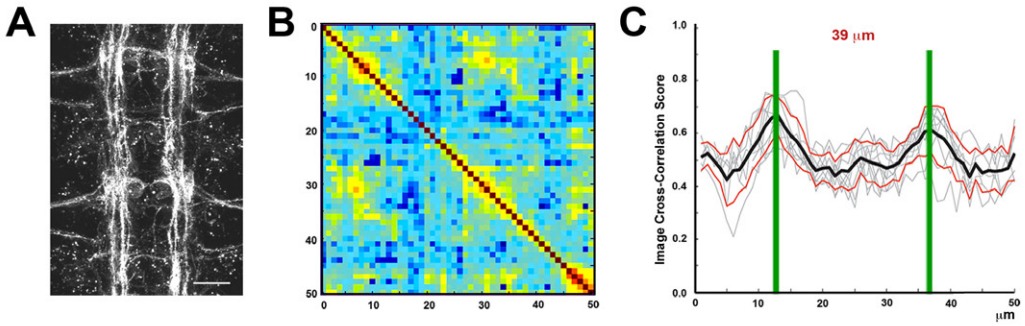

Figure S3. Robustness and modularity of the VNC architecture in *puc*^{B48} embryos

A) Maximum projection of the VNC of a *Drosophila* 16-stage *puc*^{B48} embryo stained with Fas 2. Defasciculation and collapse of longitudinal connectives is widely spread. Scale Bar is 10 µm.

B) Self cross-correlation matrix of **A**. In *puc*^{B48}, single nodes per segment are consistently developed (white arrowheads).

C) Image cross-correlation score along the A/P axis for **B**. Segmental Fas 2 nodes are on average at 24 µm from each other in *puc*^{B48} and the internodal profile flattens.

bioRxiv preprint doi: https://doi.org/10.1101/092486; this version posted December 8, 2016. The copyright holder for this preprint (which was not certified by peer review) is the author/funder, who has granted bioRxiv a license to display the preprint in perpetuity. It is made available under aCC-BY-ND 4.0 International license.

Figure S4

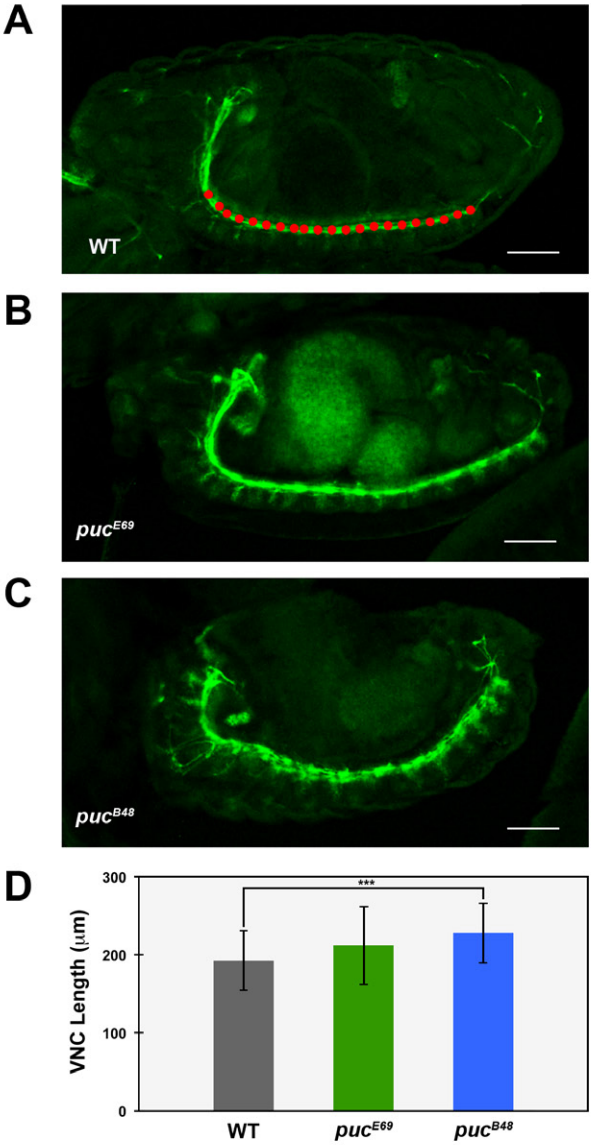

Figure S4. Loss of VNC condensation in *puc* mutants

A) *wt*, **B)** puc^{E69} and **C)** puc^{B48} embryos Fas 2 immunoreactivity. Lateral view of whole mounts of stage 17 embryos. Direct measurements of the VNC length were performed along the outline of the abdominal segments of the VNC as shown in A (dotted red line). Scale Bar is 10 μm.

D) Quantification of the VNC in μm (average and standard deviation) for each condition. Statistically significant differences in length ($p < 0.001$) were detected between the *wt* and puc^{B48} embryos. The length of the VNC of puc^{E69} embryos showed a tendency to be consistently longer than the *wt*, although it was not statistically significant.

bioRxiv preprint doi: https://doi.org/10.1101/092486; this version posted December 8, 2016. The copyright holder for this preprint (which was not certified by peer review) is the author/funder, who has granted bioRxiv a license to display the preprint in perpetuity. It is made available under aCC-BY-ND 4.0 International license.

Figure S5

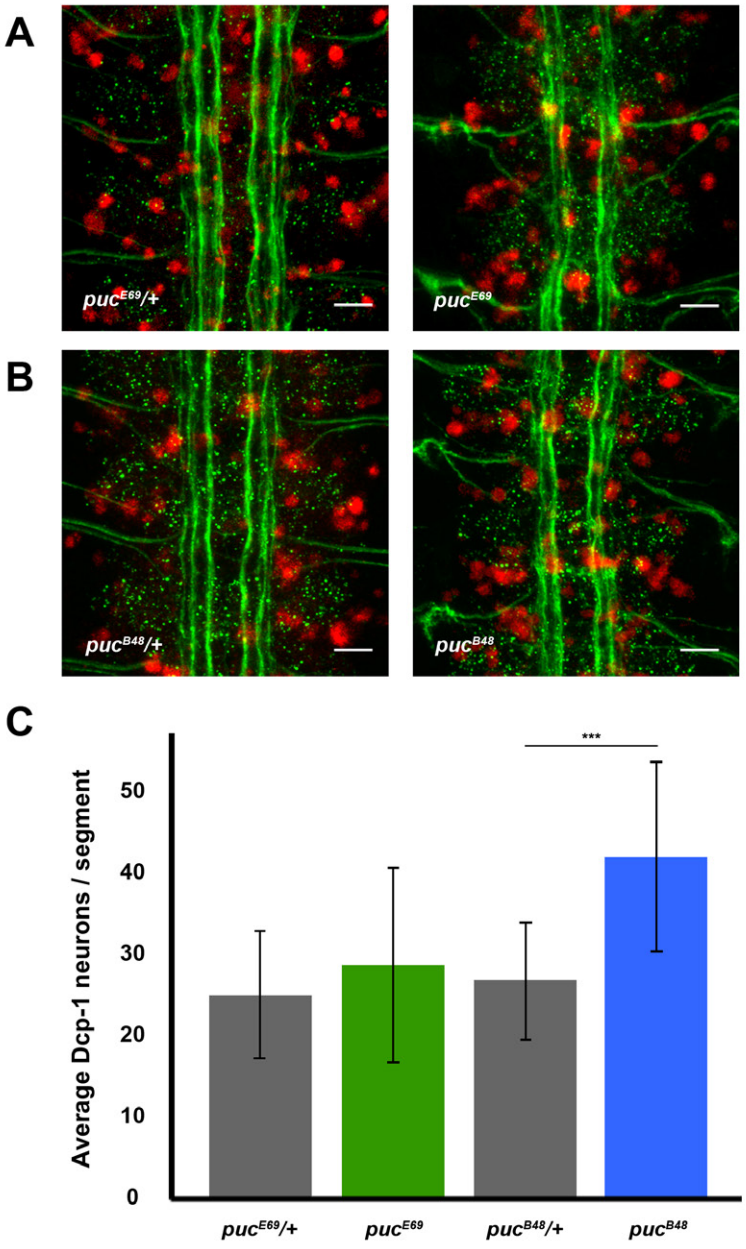

Figure S5. Cell death in *puc* mutants

A) From left to right, stage 17 heterozygous and homozygous puc^{E69} embryo stained for Fas 2 (green) and Dcp1 (red), which highlights those cells in the process of apoptosis. Scale Bar is 10 µm.

B) From left to right, equivalent images as in **A** for the puc^{B48} allele. Scale Bar is 10 µm.

bioRxiv preprint doi: https://doi.org/10.1101/092486; this version posted December 8, 2016. The copyright holder for this preprint (which was not certified by peer review) is the author/funder, who has granted bioRxiv a license to display the preprint in perpetuity. It is made available under aCC-BY-ND 4.0 International license.

C) Graph displaying the averaged Integrated Density per segment for the Dpc1 signal. Statistically significant differences in Dcp1 levels ($p < 0.001$) were detected between *wt* and *puc*^{B48} embryos. The Dpc1 levels of *puc*^{E69} embryos showed a tendency to be consistently larger than in the *wt*, although they were not statistically significant.

Figure S6

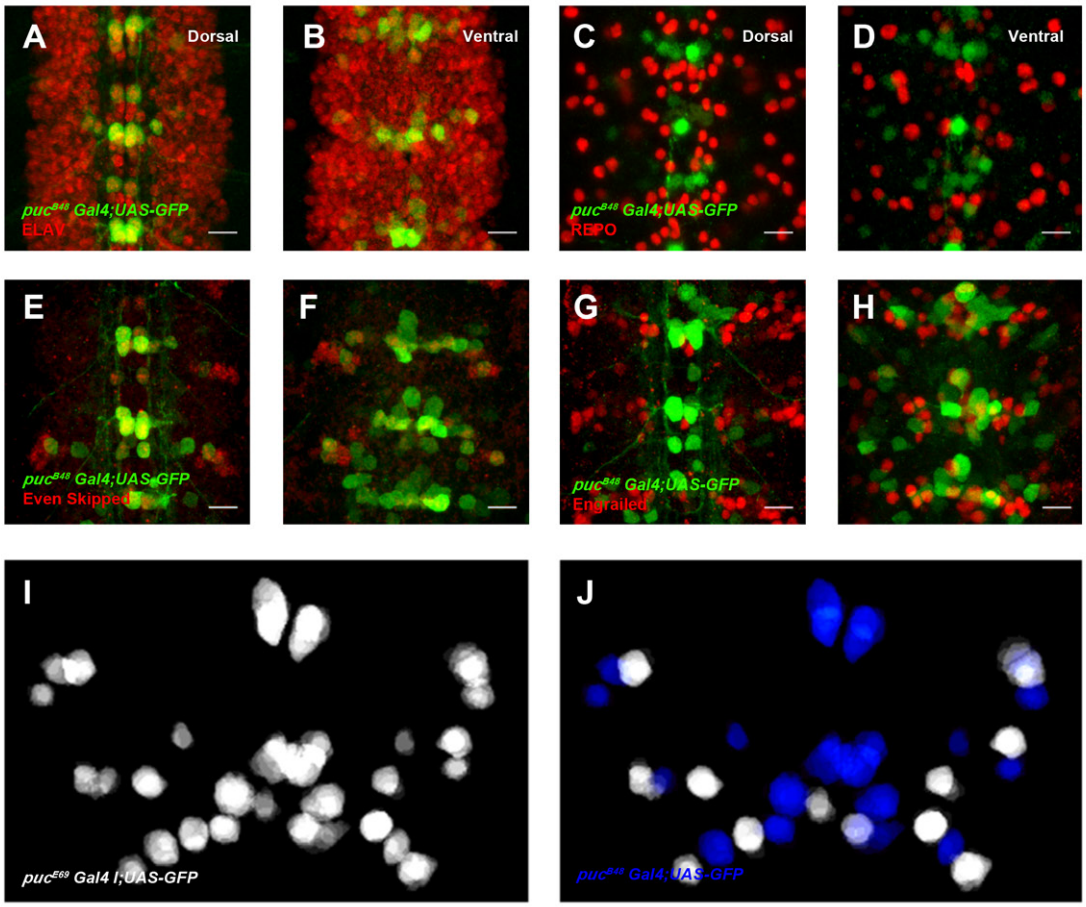

Figure S6. VNC expression of *puc*^{B48}

A to **D)** Dorsal and ventral sections highlighting the expression of *puc* (green) in the VNC of stage 17 UAS-GFP; *puc*^{B48}-Gal4 embryo double-stained for the pan-neuronal marker Elav (**A** and **B** - red) or the glial marker Repo (**C** and **D** - red). *puc* is expressed in a subset of neurons in each segments but not in glia. Scale Bar is 10 µm.

E to **H)** Dorsal and ventral sections highlighting the expression of *puc* (green) in the VNC of

bioRxiv preprint doi: https://doi.org/10.1101/092486; this version posted December 8, 2016. The copyright holder for this preprint (which was not certified by peer review) is the author/funder, who has granted bioRxiv a license to display the preprint in perpetuity. It is made available under aCC-BY-ND 4.0 International license.

stage 17 UAS-GFP; *puc*^{B48}-Gal4 embryo double-stained for Even-Skipped (**E** and **F** - red) or Engrailed (**G** and **H** - red). Scale Bar is 10 µm.

I) Cartoon representing the full set of *puc*^{B48} expressing neurons per segment in the VNC.

J) Cartoon representing the *puc*^{E69} neurons highlighting the cells expressing *puc*^{B48} (deep blue).

Figure S7

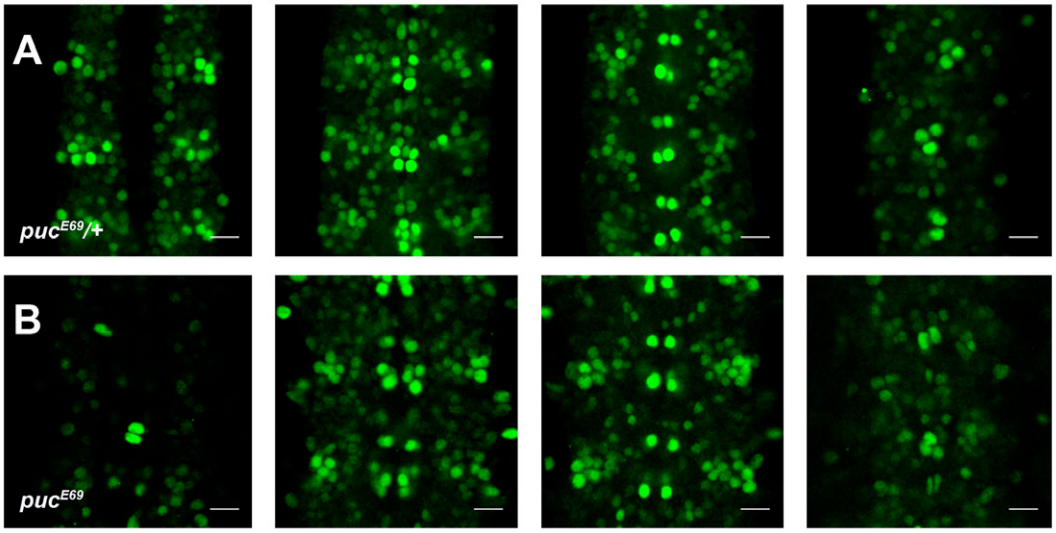

Figure S7. Zfh1 expression regulation by *puc*

A and **B)** From left to right, four 5 mm spaced Z sections of the VNC of stage 16 heterozygous (**A**) and homozygous (**B**) *puc*^{E69} embryos stained for Zfh1. Zfh1 is specifically downregulated in specific subsets of cells in homozygous animals. Scale Bar is 10 µm.

bioRxiv preprint doi: https://doi.org/10.1101/092486; this version posted December 8, 2016. The copyright holder for this preprint (which was not certified by peer review) is the author/funder, who has granted bioRxiv a license to display the preprint in perpetuity. It is made available under aCC-BY-ND 4.0 International license.

SUPPLEMENTAL MOVIES LEGENDS

Movie S1. *Drosophila* pan-axonal Network

Animated 3D reconstruction of the axonal pattern of a section of the VNC of a late *Drosophila* embryo (Stage 17) stained with anti Acetylated α-Tubulin antibodies.

Movie S2. *Drosophila* Fas 2 positive connectives

Animated 3D reconstruction of the Fas 2 positive connectives of a section of the VNC of a late *Drosophila* embryo (Stage 17).

Movie S3. *Drosophila* Fas 2 positive connectives of a puc^{E69} embryo

Animated 3D reconstruction of the Fas 2 positive connectives of a section of the VNC of a late *Drosophila* puc^{E69} mutant embryo (Stage 17).

Movie S4. Dynamics of puc^{E69} *expression*

Time course of puc^{E69} *expression* from a UAS-GFP; puc^{E69}*I*-Gal4 viable line. *puc* expression can be observed from early stage 13 in a few neurons at the midline. As development progressed, more and more neurons express *puc*, both within the VNC and at the peripheral nervous system (PNS). Anterior is to the left.

Movie S5. Minimum consensus for the segmental puc^{E69} *expression*

Animated 3D cartoon representing a single segment of a late *Drosophila* puc^{E69} mutant embryo (Stage 17). The 19 *puc* expressing cells per hemisegment represented in the minimum consensus are shown in different colors.

Movie S6. Zfh1 expression in wt and puc^{E69} mutant embryos

Animated 3D reconstruction of the Zfh1 expressing cells from *wt* (red) and puc^{E69} mutant embryos (green). Observe the larger intersegment distance between sequential segments in the mutant VNCs and the lack of Zfh1 expression in different subsets of cells within the VNC.

bioRxiv preprint doi: https://doi.org/10.1101/092486; this version posted December 8, 2016. The copyright holder for this preprint (which was not certified by peer review) is the author/funder, who has granted bioRxiv a license to display the preprint in perpetuity. It is made available under aCC-BY-ND 4.0 International license.

SUPPLEMENTAL REFERENCES

Landgraf M, Bossing T, Technau GM, Bate M (1997) The origin, location, and projections of the embryonic abdominal motorneurons of Drosophila. The Journal of neuroscience 17: 9642-55

Martin-Blanco E, Gampel A, Ring J, Virdee K, Kirov N, Tolkovsky AM, Martinez-Arias A (1998) puckered encodes a phosphatase that mediates a feedback loop regulating JNK activity during dorsal closure in Drosophila. Genes & development 12: 557-70

Pastor-Pareja JC, Grawe F, Martin-Blanco E, Garcia-Bellido A (2004) Invasive cell behavior during Drosophila imaginal disc eversion is mediated by the JNK signaling cascade. Developmental cell 7: 387-99

Patel NH (1994) Imaging neuronal subsets and other cell types in whole-mount Drosophila embryos and larvae using antibody probes. Methods in cell biology 44: 445-87

Schindelin J, Arganda-Carreras I, Frise E, Kaynig V, Longair M, Pietzsch T, Preibisch S, Rueden C, Saalfeld S, Schmid B, Tinevez JY, White DJ, Hartenstein V, Eliceiri K, Tomancak P, Cardona A (2012) Fiji: an open-source platform for biological-image analysis. Nature methods 9: 676-82